Intersubband-induced spin-orbit interaction in quantum wells

Rafael S. Calsaverini,[1] Esmerindo Bernardes,[1,*] J. Carlos Egues,[1,†] and Daniel Loss[2]
[1]*Instituto de Física de São Carlos, Universidade de São Paulo, 13560-970 São Carlos, SP, Brazil*
[2]*Department of Physics, University of Basel, CH-4056 Basel, Switzerland*
(Received 10 July 2008; published 16 October 2008)

Recently, we have found an additional spin-orbit (SO) interaction in quantum wells with two subbands [Bernardes *et al.*, Phys. Rev. Lett. **99**, 076603 (2007)]. This new SO term is nonzero even in symmetric geometries, as it arises from the intersubband coupling between confined states of distinct parities, and its strength is comparable to that of the ordinary Rashba. Starting from the 8×8 Kane model, here we present a detailed derivation of this new SO Hamiltonian and the corresponding SO coupling. In addition, within the self-consistent Hartree approximation, we calculate the strength of this new SO coupling for realistic symmetric modulation-doped wells with two subbands. We consider gated structures with either a constant areal electron density or a constant chemical potential. In the parameter range studied, both models give similar results. By considering the effects of an external applied bias, which breaks the structural inversion symmetry of the wells, we also calculate the strength of the resulting induced Rashba couplings within each subband. Interestingly, we find that for double wells the Rashba couplings for the first and second subbands interchange signs abruptly across the zero bias, while the intersubband SO coupling exhibits a resonant behavior near this symmetric configuration. For completeness we also determine the strength of the Dresselhaus couplings and find them essentially constant as function of the applied bias.

DOI: 10.1103/PhysRevB.78.155313 PACS number(s): 72.25.Dc, 71.70.Ej, 73.21.Fg, 85.75.−d

I. INTRODUCTION

The coupling between spatial and spin degrees of freedom in semiconductors provides an interesting possibility for coherently manipulating the electron spin via its orbital (charge) motion. For instance, the proposal of Datta and Das[1] for a spin field-effect transistor highlights the use of the spin-orbit (SO) interaction of Rashba,[2–4] which is electrically tunable,[5,6] to control—via spin rotation—the flow of electrons between ferromagnetic source and drain.

In addition to the Rashba SO coupling present in heterostructures with structural inversion asymmetry in the confining potential, there is the Dresselhaus SO interaction[7] present in both bulk and confined structures with inversion asymmetry in the underlying crystal lattice. These spin-orbit interactions have played an important role in the exciting field of semiconductor spintronics as they underlie a number of interesting physical phenomena and potential spintronic applications.[8–10] For instance, the effective *zitterbewegung* of spin-polarized wave packets injected into SO coupled two-dimensional (2D) electron gases is a very interesting possibility.[11,12] The interplay of the Rashba and Dresselhaus interactions can give rise to conserved spin-rotation symmetries[13,14] relevant for devising robust SO-based devices operating in the nonballistic regime.[13]

Recently, a new type of SO interaction arising in quantum confined systems with two subbands has been found.[15] Unlike the usual Rashba SO, this new SO term is nonzero even in wells with full structural inversion symmetry (and hence it does not produce spin splitting). This essentially follows from the distinct parities of the confined states (even and odd), which can couple via the derivative of a symmetric potential. This intersubband-induced SO coupling is quadratic in the crystal momentum, unlike the Rashba and the (linearized) Dresselhaus terms in wells.[16] As shown in Ref. 15, this SO coupling can give rise to an unusual *zitterbewegung* (both in position and in spin[17]) and a nonzero spin Hall conductivity.

Here we complement and extend the work of Ref. 15: (i) We present a more thorough derivation of the intersubband-induced SO interaction, starting from the 8×8 Kane model[18–20] within the $\mathbf{k}\cdot\mathbf{p}$ approach. We also slightly generalize the derivation for confined systems with more than two subbands and *structurally asymmetric* potentials in which the usual Rashba-type SO interaction is present. (ii) We perform a detailed investigation of the relevant SO couplings via a self-consistent scheme where we solve both Poisson and Schrödinger equations numerically (Numerov method) within the Hartree approximation. We consider realistic modulation-doped single and double quantum wells with applied external biases, which can change the spatial symmetry of the wells, and having either a constant areal electron density or a constant chemical potential.

Our simulations focus on wells with two subbands. For nonzero applied biases we calculate not only the intersubband-induced SO coupling η but also the Rashba-type couplings α_0, α_1 for the first and second subbands, respectively. For completeness, we also calculate the linearized Dresselhaus SO couplings for each subband.[21] For both the constant density and constant chemical-potential models considered, we find sizable values of the intersubband SO coupling η as compared to the usual Rashba and Dresselhaus couplings. Interestingly, for double wells near the symmetric (zero-bias) configuration we find that η has a resonant behavior, changing its magnitude by a factor of 10. On the other hand, the Rashba couplings for the first and second subbands abruptly change signs around the zero-bias voltage. The Dresselhaus couplings do not show any noticeable behavior around this point, being essentially constant as a function of the applied bias.

 ©2008 The American Physical Society

We note that the SO coupling constants η, α_0, and α_1 contain contributions from the potential-well (and barrier) offsets, the electronic Hartree potential, and the external gate plus the modulation doping potentials. For the *single wells* investigated here, the external gate (+ modulation doping) is the dominant contribution to α_0 and α_1, while η is mostly determined by the Hartree and structural offset contributions. On the other hand, for the *double wells* studied the electronic Hartree potential is the dominant contribution to η, α_0, and α_1. Interestingly, the Hartree potential in this case is highly influenced by the external gate, particularly around the symmetric (zero-bias) configuration, as the electrons can localize in either well for small (positive or negative) changes in the gate potential. This renders η, α_0, and α_1 more amenable to gate modulations in double wells as compared to single wells. Next we outline our work.

In Sec. II we review the $\mathbf{k}\cdot\mathbf{p}$ approach and the Kane model. In Sec. III we present a detailed derivation of our effective Hamiltonian for electrons in heterostructures with many confined states within the Kane model. In this section we also show the relevant expressions for the new intersubband-induced SO coupling η and those for the Rashba α (and Dresselhaus β) SO couplings as well. In Sec. IV we describe the quantum wells investigated and (briefly) the standard self-consistent calculation performed. We present our results and discussions in Sec. V. In this section we focus specifically on realistic single and double-well systems. Section VI summarizes our work. In Appendixes A and B we show details of our self-consistent scheme to solve the relevant Schrödinger and Poisson equations.

II. k·p APPROACH AND KANE MODEL

Here we briefly review the $\mathbf{k}\cdot\mathbf{p}$ approach and use it to obtain the 8×8 Kane model relevant for our derivation of the new intersubband-induced SO coupling.[19,20]

A. Basics of the k·p method

The single-particle Hamiltonian for an electron with momentum $\boldsymbol{p}$ in a periodic potential[19,22] $V(\boldsymbol{r})$ with SO is

$$H=\frac{\boldsymbol{p}^2}{2m_0}+V(\boldsymbol{r})+\frac{\hbar}{4m_0^2c^2}\boldsymbol{\sigma}\times\boldsymbol{\nabla}V(\boldsymbol{r})\cdot\boldsymbol{p}, \tag{1}$$

where m_0 is the bare electron mass and $\boldsymbol{\sigma}$ is a vector operator defined in terms of the Pauli matrices. With the help of Bloch's theorem $\psi_{n\boldsymbol{k}}(\boldsymbol{r})=\exp(i\boldsymbol{k}\cdot\boldsymbol{r})u_{n\boldsymbol{k}}(\boldsymbol{r})$ [$u_{n\boldsymbol{k}}(\boldsymbol{r})$ has the periodicity of the underlying Bravais lattice] we can rewrite the Schrödinger's equation $H\psi_{n\boldsymbol{k}}=\varepsilon_{n\boldsymbol{k}}\psi_{n\boldsymbol{k}}$, where n indexes the distinct solutions for each $\boldsymbol{k}$ vector, in the form

$$[H(\boldsymbol{k}=\boldsymbol{0})+W(\boldsymbol{k})]u_{n\boldsymbol{k}}(\boldsymbol{r})=\left(\varepsilon_{n\boldsymbol{k}}-\frac{\hbar^2k^2}{2m_0}\right)u_{n\boldsymbol{k}}(\boldsymbol{r}), \tag{2}$$

with

$$H(\boldsymbol{k}=0)=-\frac{\hbar^2}{2m_0}\nabla^2+V(\boldsymbol{r})+\frac{\hbar}{4m_0^2c^2}\boldsymbol{\sigma}\times\boldsymbol{\nabla}V(\boldsymbol{r})\cdot\boldsymbol{p}, \tag{3}$$

$$W(\boldsymbol{k})=\frac{\hbar}{m_0}\boldsymbol{k}\cdot\left(\boldsymbol{p}+\frac{\hbar}{4m_0c^2}\boldsymbol{\sigma}\times\boldsymbol{\nabla}V(\boldsymbol{r})\right). \tag{4}$$

As usual, to solve Eq. (2), we expand $u_{n\boldsymbol{k}}$ in terms of the eigenstates $u_{l\boldsymbol{0}}$ at $\boldsymbol{k}=\boldsymbol{0}$ [i.e., $W(\boldsymbol{k}=\boldsymbol{0})=0$] obtained from

$$H(\boldsymbol{k}=\boldsymbol{0})u_{l0}(\boldsymbol{r})=\varepsilon_{l\boldsymbol{0}}u_{l\boldsymbol{0}}(\boldsymbol{r}), \tag{5}$$

where $l=1,2,\ldots N$ (in principle, $N\to\infty$) indexes the discrete set of levels at $\boldsymbol{k}=\boldsymbol{0}$ [note that Eq. (5) contains the SO interaction, even though $W(\boldsymbol{0})=0$]. Substituting

$$u_{n\boldsymbol{k}}(\boldsymbol{r})=\sum_{l=1}^{N}a_{nl}(\boldsymbol{k})u_{l\boldsymbol{0}}(\boldsymbol{r}) \tag{6}$$

into Eq. (2) and projecting the resulting expression onto the $u_{l'\boldsymbol{0}}(\boldsymbol{r})$ eigenstate, we find[19]

$$\sum_{l=1}^{N}\Bigg[\left(\varepsilon_{l\boldsymbol{0}}-\varepsilon_{n\boldsymbol{k}}+\frac{\hbar^2k^2}{2m_0}\right)\delta ll' +\langle l'|\frac{\hbar}{m_0}\boldsymbol{k}\cdot\boldsymbol{p}+\frac{\hbar^2}{4m_0^2c^2}\boldsymbol{k}\cdot\boldsymbol{\sigma}\times\boldsymbol{\nabla}V(\boldsymbol{r})|l\rangle\Bigg]a_{nl}(\boldsymbol{k})=0. \tag{7}$$

Here we use the notation $\langle\boldsymbol{r}|l\rangle=u_{l\boldsymbol{0}}(\boldsymbol{r})$ and define

$$\langle l'|A|l\rangle=\int d^3r u^*_{l'\boldsymbol{0}}Au_{l\boldsymbol{0}}, \tag{8}$$

with A denoting a Hermitian operator.

B. 8×8 Kane model—bulk case

As usual, in order to solve Eq. (7) we have to truncate the basis set by considering a finite number N of zone-center basis functions $u_{l0}(\boldsymbol{r})$. In addition, since the $\boldsymbol{k}=\boldsymbol{0}$ Hamiltonian [Eq. (3)] contains a SO term, it is convenient to choose linear combinations of basis functions which are eigenstates of the total angular momentum $\mathbf{J}=\mathbf{L}+\mathbf{S}$, and its z component J_z; here $\mathbf{L}$ and $\mathbf{S}$ denote the orbital and spin angular momenta, respectively. In II-VI and III-V (both zincblend) compounds the relevant conduction and valence bands arise from the "bonding" p-type and "antibonding" s-type states, respectively. Following the notation of Refs. 19 and 23, we summarize in Table I the set of eight zone-center wave functions we consider here (the kets $|JJ_z\rangle$ are also shown), which are the eigenstates of the zone-center Schrödinger Eq. (5) for the periodic part of the Bloch function. Note that we use the standard state vector notation $|S\rangle$, $|X\rangle$, $|Y\rangle$, and $|Z\rangle$ to denote the symmetry of the corresponding "atomic orbitals" (tight-binding view).

Using the ordered basis states $u_1,\ldots,u_8$ in Table I we can easily write out the matrix Hamiltonian [Eq. (7)][19,20,24]

$$H_{8\times 8}=\begin{bmatrix} \frac{\hbar^2k^2}{2m_0} & 0 & -\frac{1}{\sqrt{2}}Pk_+ & \sqrt{\frac{2}{3}}Pk_z & \frac{1}{\sqrt{6}}Pk_- & 0 & -\frac{1}{\sqrt{3}}Pk_z & -\frac{1}{\sqrt{3}}Pk_- \\ 0 & \frac{\hbar^2k^2}{2m_0} & 0 & -\frac{1}{\sqrt{6}}Pk_+ & \sqrt{\frac{2}{3}}Pk_z & \frac{1}{\sqrt{2}}Pk_- & -\frac{1}{\sqrt{3}}Pk_+ & \frac{1}{\sqrt{3}}Pk_z \\ -\frac{1}{\sqrt{2}}Pk_- & 0 & \frac{\hbar^2k^2}{2m_0}-E_g & 0 & 0 & 0 & 0 & 0 \\ \sqrt{\frac{2}{3}}Pk_z & -\frac{1}{\sqrt{6}}Pk_- & 0 & \frac{\hbar^2k^2}{2m_0}-E_g & 0 & 0 & 0 & 0 \\ \frac{1}{\sqrt{6}}Pk_+ & \sqrt{\frac{2}{3}}Pk_z & 0 & 0 & \frac{\hbar^2k^2}{2m_0}-E_g & 0 & 0 & 0 \\ 0 & \frac{1}{\sqrt{2}}Pk_+ & 0 & 0 & 0 & \frac{\hbar^2k^2}{2m_0}-E_g & 0 & 0 \\ -\frac{1}{\sqrt{3}}Pk_z & -\frac{1}{\sqrt{3}}Pk_- & 0 & 0 & 0 & 0 & \frac{\hbar^2k^2}{2m_0}-E_g-\Delta_g & 0 \\ -\frac{1}{\sqrt{3}}Pk_+ & \frac{1}{\sqrt{3}}Pk_z & 0 & 0 & 0 & 0 & 0 & \frac{\hbar^2k^2}{2m_0}-E_g-\Delta_g \end{bmatrix}, \quad (9)$$

where P is the usual Kane matrix element[18]

$$P=-i\frac{\hbar}{m_0}\langle S|p_x|X\rangle=\hbar\sqrt{\frac{E_P}{2m_0}}, \quad (10)$$

expressed in terms of the parameter E_P (Ref. 25) and $k_\pm=k_x\pm ik_y$. We have also used that $\langle S|p_x|X\rangle=\langle S|p_y|Y\rangle=\langle S|p_z|Z\rangle$. Equation (9) is the 8×8 Kane Hamiltonian[18] describing the s-type conduction and p-type valence bands around the Γ point in zincblend compounds. Note that the diagonal elements in Hamiltonian (9) correspond to the eigenenergies $\varepsilon_{l\mathbf{0}}$ of Eq. (5): $\varepsilon_{1\mathbf{0}}=\varepsilon_{2\mathbf{0}}=0$ ("conduction-band states," defined as the zero of energy), $\varepsilon_{3\mathbf{0}}=\varepsilon_{4\mathbf{0}}=\varepsilon_{5\mathbf{0}}=\varepsilon_{6\mathbf{0}}=-E_g$ ("heavy" and "light" hole bands), and $\varepsilon_{7\mathbf{0}}=\varepsilon_{8\mathbf{0}}=-E_g-\Delta_g$ ("split-off" hole band). Here,

TABLE I. Truncated set of zone-center wave functions $u_{l\mathbf{0}}$ (for simplicity we denote them by u_l) used in constructing the matrix Hamiltonian (9).

u_i	Γ	$\lvert J,m_J\rangle$	u_{J,m_J}
u_1	Γ_6	$\lvert\frac{1}{2},+\frac{1}{2}\rangle$	$i\lvert S\rangle\otimes\lvert+\frac{1}{2}\rangle$
u_2	Γ_6	$\lvert\frac{1}{2},-\frac{1}{2}\rangle$	$i\lvert S\rangle\otimes\lvert-\frac{1}{2}\rangle$
u_3	Γ_8	$\lvert\frac{3}{2},+\frac{3}{2}\rangle$	$-\frac{1}{\sqrt{2}}(\lvert X\rangle+i\lvert Y\rangle)\otimes\lvert+\frac{1}{2}\rangle$
u_4	Γ_8	$\lvert\frac{3}{2},+\frac{1}{2}\rangle$	$-\frac{1}{\sqrt{6}}(\lvert X\rangle+i\lvert Y\rangle)\otimes\lvert-\frac{1}{2}\rangle+\sqrt{\frac{2}{3}}\lvert Z\rangle\otimes\lvert+\frac{1}{2}\rangle$
u_5	Γ_8	$\lvert\frac{3}{2},-\frac{1}{2}\rangle$	$+\frac{1}{\sqrt{6}}(\lvert X\rangle-i\lvert Y\rangle)\otimes\lvert+\frac{1}{2}\rangle+\sqrt{\frac{2}{3}}\lvert Z\rangle\otimes\lvert-\frac{1}{2}\rangle$
u_6	Γ_8	$\lvert\frac{3}{2},-\frac{3}{2}\rangle$	$+\frac{1}{\sqrt{2}}(\lvert X\rangle-i\lvert Y\rangle)\otimes\lvert-\frac{1}{2}\rangle$
u_7	Γ_7	$\lvert\frac{1}{2},+\frac{1}{2}\rangle$	$-\frac{1}{\sqrt{3}}(\lvert X\rangle+i\lvert Y\rangle)\otimes\lvert-\frac{1}{2}\rangle-\frac{1}{\sqrt{3}}\lvert Z\rangle\otimes\lvert+\frac{1}{2}\rangle$
u_8	Γ_7	$\lvert\frac{1}{2},-\frac{1}{2}\rangle$	$-\frac{1}{\sqrt{3}}(\lvert X\rangle-i\lvert Y\rangle)\otimes\lvert+\frac{1}{2}\rangle+\frac{1}{\sqrt{3}}\lvert Z\rangle\otimes\lvert-\frac{1}{2}\rangle$

$$\Delta_g=\frac{3\hbar^2}{4m_0^2c^2}\langle X|\frac{\partial V}{\partial y}\frac{\partial}{\partial x}-\frac{\partial V}{\partial x}\frac{\partial}{\partial y}|Y\rangle \quad (11)$$

is the "atomic" SO parameter defining the split-off gap; see Fig. 1(a). Figure 1(a) schematically shows the conduction and valence bands of a zincblend structure. The circles indicate the $\boldsymbol{k}=\mathbf{0}$ eigenenergies.

The Kane model treats exactly the conduction-valence-band couplings within the truncated set of eight band-edge wave functions. It is important to emphasize that we have neglected contributions from the $\boldsymbol{k}$-dependent SO term in Eq. (7), when constructing the Kane Hamiltonian (9).[18] The SO interaction is accounted for only within the zone-center Schrödinger Eq. (5) (parameter Δ_g above). The diagonalization of the Kane Hamiltonian gives the dispersions $\varepsilon_{n,\boldsymbol{k}}$ around the Γ point. It is known that the Kane model presented here is not accurate for valence bands[19] (e.g., wrong sign of the heavy hole masses). However, it provides a simplified and accurate description for the conduction electrons, which is the focus of our work. Next we discuss the Kane model in the context of heterostructures.

C. Kane model for quantum wells

Following Refs. 19 and 20 we can straightforwardly generalize the bulk Kane model of Sec. II B to heterostructures. Essentially, we have to introduce position-dependent (growth direction) band gaps which represent the different compounds comprising the heterostructure, e.g., Fig. 1(b). In this case, the form of the resulting Kane Hamiltonian is similar to that of bulk but with z-dependent diagonal matrix elements and with $k_z\to -id/dz$. More specifically, defining $E_6=H_{11}=H_{22}$, $E_8=H_{33}=H_{44}=H_{55}=H_{66}$, and $E_7=H_{77}=H_{88}$, we have for the double quantum well of Fig. 1(b)

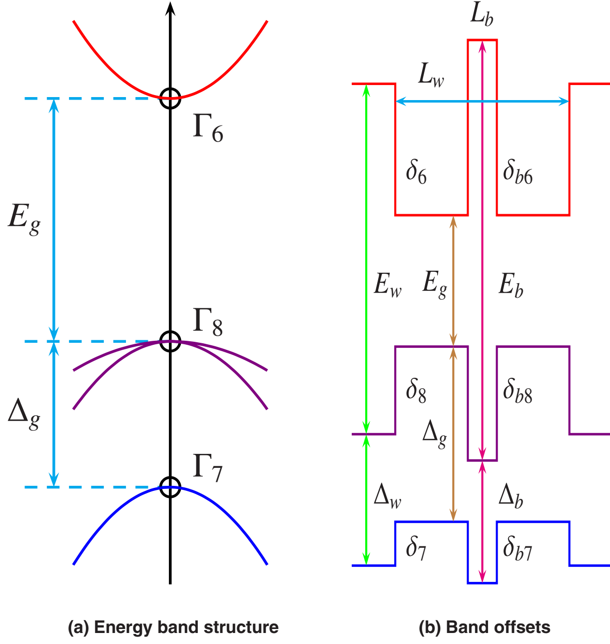

FIG. 1. (Color online) (a) Schematic of the band structure of direct gap zincblend semiconductors near the Γ point (k=0). The label Γ_6 represents the s states in the conduction band, while Γ_7 (split-off holes) and Γ_8 (heavy holes and light holes) represent the p states in the valence bands. (b) Band offsets for a double quantum well of width L_w with a central barrier of width L_b. The relationships among the several offset parameters are given in Eqs. (16) and (17).

$$E_6 = \frac{\hbar^2 k^2}{2m_0} + V_H(z) + h_6(z), \quad (12)$$

$$E_8 = \frac{\hbar^2 k^2}{2m_0} + V_H(z) - h_8(z) - E_g, \quad (13)$$

$$E_7 = \frac{\hbar^2 k^2}{2m_0} + V_H(z) - h_7(z) - E_g - \Delta_g, \quad (14)$$

with $k^2 = k_\parallel^2 + k_z^2$, E_g and Δ_g being the fundamental and split-off band gaps in the well region, respectively, and

$$h_i(z) = \delta_i h_w(z) + \delta_{bi} h_b(z), \quad i = 6,7,8, \quad (15)$$

where $h_w(z)$ is a dimensionless profile function describing the shape of a square well of width L_w [and unit depth, Fig. 1(b)]; similarly, $h_b(z)$ describes the shape of the central square barrier, Fig. 1(b). The parameters δ_6, δ_7, δ_8, δ_{b6}, δ_{b7}, and δ_{b8} denote the relevant band offsets between the well and the lateral and central barriers for conduction and valence bands. Defining the zero of energy at the bottom of the conduction well [see Fig. 1(b)], we have

$$\delta_8 = E_w - E_g - \delta_6, \quad \delta_7 = \delta_8 + \Delta_w - \Delta_g, \quad (16)$$

$$\delta_{b8} = E_b - E_g - \delta_{b6}, \quad \delta_{b7} = \delta_{b8} + \Delta_b - \Delta_g. \quad (17)$$

The corresponding expressions for a single well can readily be obtained from the above by setting the δ_{bi}'s to zero (i.e., no central barrier).

Finally, note that we have added a "Hartree" potential $V_H(z)$ in the diagonal elements; see Eqs. (12)–(14). The Hartree potential $V_H(z)$ here contains contributions from the electron-electron interaction (mean field) relevant in quantum wells containing many electrons, the external gate potentials, and the modulation-doped potential (i.e., ionized impurities outside the well region). In Appendix A, we describe in detail these distinct contributions to V_H and how they are calculated in our system. As we will see next, both $V_H(z)$ and the structural confining potentials contribute to the effective SO coupling for electrons.

III. EFFECTIVE SPIN-ORBIT HAMILTONIAN FOR ELECTRONS

A. Folding down

Since we are interested in SO effects for the conduction electrons, here we derive an effective Hamiltonian for them. To this end, let us rewrite our 8×8 Hamiltonian [Eq. (9)] in the block form

$$H_{8\times8} = \begin{pmatrix} H_c & H_{cv} \\ H_{cv}^\dagger & H_v \end{pmatrix}, \quad (18)$$

where H_c is a 2×2 diagonal matrix in the sector Γ_6 (conduction band) with identical diagonal elements E_6 [Eq. (12)] and H_v is a 6×6 diagonal matrix in the sectors Γ_8 and Γ_7 (valence bands) with diagonal elements E_8 [Eq. (13)] and E_7 [Eq. (14)], respectively. The 2×6 matrix H_{cv} can be read off directly from the corresponding 2×6 block in Eq. (9).

Using the block form of our Hamiltonian (18) the eigenvalue problem can be written in the compact form

$$\begin{pmatrix} H_c & H_{cv} \\ H_{cv}^\dagger & H_c \end{pmatrix}\begin{pmatrix} \varphi_c \\ \varphi_v \end{pmatrix} = E\begin{pmatrix} \varphi_c \\ \varphi_v \end{pmatrix}, \quad (19)$$

where φ_c is a two-component spinor (conduction sector) and φ_v is a six-component spinor (valence sector). Straightforward manipulations[19,20] yield the effective Schrödinger-type equation

$$\mathcal{H}(E)\tilde{\varphi}_c = E\tilde{\varphi}_c, \quad (20)$$

with

$$\mathcal{H}(E) = H_c + H_{cv}(E - H_v)^{-1}H_{cv}^\dagger, \quad (21)$$

and $\tilde{\varphi}_c$ is a properly renormalized conduction-electron spinor.[26]

The matrix elements of $\mathcal{H}(E)$ are given by[27]

$$\mathcal{H}(E)_{11} = \mathcal{H}(E)_{22} = E_6 + \frac{P^2}{3}(k_\parallel^2\gamma_1 + k_z\gamma_1 k_z), \quad (22)$$

$$\mathcal{H}(E)_{12} = \mathcal{H}(E)_{21}^\dagger = \frac{P^2}{3}k_-[\gamma_2, k_z] = -\frac{P^2}{3}k_- k_z \gamma_2, \quad (23)$$

where $k_\parallel^2 = k_\pm k_\mp = k_x^2 + k_y^2$ and

$$\gamma_1(z) = \left(\frac{2}{E - E_8} + \frac{1}{E - E_7}\right), \quad (24)$$

$$\gamma_2(z) = \left(\frac{1}{E-E_8} - \frac{1}{E-E_7}\right). \tag{25}$$

We should emphasize that Eq. (20) is not really an eigenvalue equation as $\mathcal{H}(E)$ depends on E. However, as we show in Sec. III B, we can still obtain a true eigenvalue problem by performing suitable expansions.

B. Energy denominator expansions

Since E_g and $E_g+\Delta$ are the largest energy scales in our system, i.e.,

$$\chi_8 = \frac{E - \left[\frac{\hbar^2 k^2}{2m_0} + V_H(z) - h_8(z)\right]}{E_g} \ll 1, \tag{26}$$

$$\chi_7 = \frac{E - \left[\frac{\hbar^2 k^2}{2m_0} + V_H(z) - h_7(z)\right]}{E_g + \Delta_g} \ll 1, \tag{27}$$

we can expand the energy denominators in the γ_i's [Eqs. (24) and (25)] in the form

$$\gamma_1 = \frac{2}{E_g}(1 - \chi_8 + \cdots) + \frac{1}{E_g+\Delta_g}(1-\chi_7+\cdots), \tag{28}$$

$$\gamma_2 = \frac{1}{E_g}(1 - \chi_8 + \cdots) - \frac{1}{E_g+\Delta_g}(1-\chi_7+\cdots). \tag{29}$$

For the diagonal matrix elements $\mathcal{H}(E)_{11}=\mathcal{H}(E)_{22}$ we keep only zeroth-order (i.e., energy-independent) terms, while for the off-diagonal matrix elements $\mathcal{H}(E)_{12}=\mathcal{H}(E)_{21}^{\dagger}$ we keep in addition the first-order terms as they give the lowest nonvanishing contribution (because the off-diagonal matrix elements contain derivatives with respect to z). Straightforwardly, we then obtain the *energy-independent* electron Hamiltonian

$$\mathcal{H}(E) = H_{\mathrm{QW}}\mathbf{1} + \eta(z)\begin{pmatrix} 0 & -ik_- \\ ik_+ & 0 \end{pmatrix}, \tag{30}$$

where

$$H_{\mathrm{QW}} = \frac{\hbar^2 k_\parallel^2}{2m^*} + \frac{\hbar^2}{2m^*}\frac{\partial^2}{\partial z^2} + V_{\mathrm{sc}}(z), \tag{31}$$

[the subscript "sc" emphasizes that the potential is to be determined self-consistently—see Appendixes A and B] and[15]

$$\frac{1}{m^*} = \frac{1}{m_0} + \frac{2P^2}{3\hbar^2}\left(\frac{2}{E_g} + \frac{1}{E_g+\Delta_g}\right), \tag{32}$$

$$V_{\mathrm{sc}}(z) = V_H(z) + \delta_6 h_w(z) + \delta_{b6} h_b(z), \tag{33}$$

$$\eta(z) = \eta_w \frac{dh_w(z)}{dz} + \eta_b \frac{dh_b(z)}{dz} - \eta_H \frac{dV_H(z)}{dz}, \tag{34}$$

with

$$\eta_H = \frac{P^2}{3}\left[\frac{1}{E_g^2} - \frac{1}{(E_g+\Delta_g)^2}\right], \tag{35}$$

$$\eta_w = \frac{P^2}{3}\left[\frac{\delta_8}{E_g^2} - \frac{\delta_7}{(E_g+\Delta_g)^2}\right], \tag{36}$$

$$\eta_b = \frac{P^2}{3}\left[\frac{\delta_{b8}}{E_g^2} - \frac{\delta_{b7}}{(E_g+\Delta_g)^2}\right]. \tag{37}$$

C. Projection into the quantum-well subbands

Here we define a quasi-two-dimensional model starting from the three-dimensional (3D) Hamiltonian (30). The idea is essentially to obtain a 2D effective model similar to the well-known Rashba model, but now for the case of wells with many subbands. To this end we (i) first project Eq. (30) into the spin-degenerate eigenstates of H_{QW} [Eq. (31)] (note that H_{QW} *does not* contain the SO interaction):[28] $|\mathbf{k}_\parallel \nu\rangle_{\sigma_z} = |\mathbf{k}_\parallel \nu\rangle|\sigma_z\rangle$, $\langle \mathbf{r}|\mathbf{k}_\parallel \nu\rangle = \exp(i\mathbf{k}_\parallel \cdot \mathbf{r}_\parallel)\varphi_\nu(z)$, $\nu=0,1,2,\ldots$, and $\sigma_z = \pm$ (or $\uparrow,\downarrow$), which correspond to the subband energies $\mathcal{E}_{k_\parallel \nu} = \frac{\hbar^2 k_\parallel^2}{2m^*} + \mathcal{E}_\nu$, with $\mathcal{E}_\nu$ being the quantized levels of the well, and then (ii) consider a reduced set of subbands (e.g., two) by truncating the basis set used. In this section we simply assume that we know the eigensolutions of H_{QW}; later on we actually calculate them within a self-consistent procedure, from which we can explicitly determine the relevant SO coupling constants in our problem.

The matrix elements of $\mathcal{H}(\varepsilon)$ in the $\{|\mathbf{k}_\parallel \nu\rangle_{\sigma_z}\}$ basis are

$$\langle \mathbf{k}_\parallel \nu|\langle \pm|\mathcal{H}(E)|\mathbf{k}_\parallel \nu'\rangle|\pm\rangle = \left(\frac{\hbar^2 k_\parallel^2}{2m^*} + \mathcal{E}_\nu\right)\delta_{\nu\nu'}, \tag{38}$$

$$\langle \mathbf{k}_\parallel \nu|\langle \pm|\mathcal{H}(E)|\mathbf{k}_\parallel \nu'\rangle|\mp\rangle = \mp i\eta_{\nu\nu'}k_\mp, \tag{39}$$

with the generalized SO couplings

$$\eta_{\nu\nu'} = \Gamma^H_{\nu\nu'} + \Gamma^w_{\nu\nu'} + \Gamma^b_{\nu\nu'}, \tag{40}$$

where

$$\Gamma^H_{\nu\nu'} = -\eta_H\langle \nu|\frac{dV_H(z)}{dz}|\nu'\rangle, \tag{41}$$

$$\Gamma^w_{\nu\nu'} = +\eta_w\langle \nu|\frac{dh_w(z)}{dz}|\nu'\rangle, \tag{42}$$

$$\Gamma^b_{\nu\nu'} = +\eta_b\langle \nu|\frac{dh_b(z)}{dz}|\nu'\rangle. \tag{43}$$

The coefficients $\Gamma^H_{\nu\nu'}$, $\Gamma^w_{\nu\nu'}$, and $\Gamma^b_{\nu\nu'}$ denote the contributions from the Hartree potential, the quantum-well edges, and the central barrier edges, respectively. It is convenient to split the Hartree contribution into two terms, i.e., $V_H(z)=V_e(z)+V_g(z)$, where $V_e(z)$ is the purely electronic Hartree potential and $V_g(z)$ denotes the contributions from the external gate potential and the modulation doping potential. Hence $\Gamma^{(H)}_{\nu\nu'} = -\eta_H\langle \nu|\frac{dV_e(z)}{dz}|\nu'\rangle - \eta_H\langle \nu|\frac{dV_g(z)}{dz}|\nu'\rangle$. This separation will be useful when discussing our results.

We emphasize that the diagonal (in ν,ν') parameters $\eta_{\nu\nu}$ correspond to the Rashba coupling in the νth subband, i.e.,

$\alpha_v = \eta_{vv}$. The off-diagonal terms $\eta_{vv'}$ arise due to the intersubband coupling. Interestingly, these new SO terms can be nonzero even in structurally symmetric wells, since they arise from quantum-well states of distinctive parities.

For completeness we present here the linearized Dresselhaus couplings[29] in the vth subband

$$\beta_v = \beta_D \langle v | k_z^2 | v \rangle, \tag{44}$$

where the constant β_D is the bulk Dresselhaus SO parameter.[21] We can easily rewrite the above expression in the more convenient form

$$\beta_v = \beta_D \frac{2m^*}{\hbar^2} [\mathcal{E}_v - \langle v | V(z) | v \rangle]. \tag{45}$$

In Sec. V we shall use the above form to discuss how the Dresselhaus couplings vary as a function of the system parameters.

D. Two-subband case

To illustrate the procedure of Sec. III C, let us explicitly work out here the case of a quantum well with only two subbands $v=0,1$. In Sec. V we shall investigate in detail the SO couplings for single and double quantum wells with two subbands.

1. 4×4 *Hamiltonian*

With the basis ordering $\{|\mathbf{k}_\parallel 0\rangle_\uparrow, |\mathbf{k}_\parallel 0\rangle_\downarrow, |\mathbf{k}_\parallel 1\rangle_\uparrow, |\mathbf{k}_\parallel 1\rangle_\downarrow\}$, Eqs. (38) and (39) yield the effective Hamiltonian

$$H = \begin{pmatrix} \mathcal{E}_{k_\parallel 0} & -i\alpha_0 k_- & 0 & -i\eta k_- \\ i\alpha_0 k_+ & \mathcal{E}_{k_\parallel 0} & i\eta k_+ & 0 \\ 0 & -i\eta k_- & \mathcal{E}_{k_\parallel 1} & -i\alpha_1 k_- \\ i\eta k_+ & 0 & i\alpha_1 k_+ & \mathcal{E}_{k_\parallel 1} \end{pmatrix}, \tag{46}$$

where the Rashba couplings are given by $\alpha_v = \eta_{vv}$, $v=0,1$, and the intersubband SO coupling[30] by $\eta = \eta_{01}$ [see Eqs. (40)–(43)] and

$$\mathcal{E}_{k_\parallel v} = \mathcal{E}_v + \frac{(\hbar k_\parallel)^2}{2m^*}, \quad v=0,1. \tag{47}$$

2. *Eigensolutions*

The energy eigenvalues $\mathcal{E}_{\sigma\lambda}$ of Eq. (46) are straightforward to obtain:

$$\mathcal{E}_{k_\parallel,\lambda_1,\lambda_2} = \mathcal{E}_{k_\parallel +} + \lambda_2 \alpha_+ k_\parallel + \lambda_1 \sqrt{(\eta k_\parallel)^2 + (\mathcal{E}_{k_\parallel -} + \lambda_2 \alpha_- k_\parallel)^2}, \tag{48}$$

where $\lambda_2 = \pm$ are spin quantum numbers and $\lambda_1 = \pm$ are the subband (or pseudospin) indices, and

$$\mathcal{E}_{k_\parallel \pm} = \frac{1}{2}(\mathcal{E}_{k_\parallel 1} \pm \mathcal{E}_{k_\parallel 0}), \quad \alpha_\pm = \frac{1}{2}(\alpha_1 \pm \alpha_0). \tag{49}$$

The corresponding (normalized) eigenvectors are

$$\langle \mathbf{r}_\parallel | \mathbf{k}_\parallel, \lambda_1, \lambda_2 \rangle = \sqrt{1 + \lambda_1 \frac{\epsilon_{\lambda_2}(0)}{\epsilon_{\lambda_2}(\eta)}} \begin{pmatrix} \dfrac{-i\lambda_1 \eta k_\parallel e^{-i\theta}}{\epsilon_{\lambda_2}(\eta) + \lambda_1 \epsilon_{\lambda_2}(0)} \\ \dfrac{\lambda_1 \lambda_2 \eta k_\parallel}{\epsilon_{\lambda_2}(\eta) + \lambda_1 \epsilon_{\lambda_2}(0)} \\ -i\lambda_2 e^{-i\theta} \\ 1 \end{pmatrix} \frac{e^{i\mathbf{k}_\parallel \cdot \mathbf{r}_\parallel}}{4\pi}, \tag{50}$$

where

$$\epsilon_\pm(\eta) = \sqrt{(\eta k_\parallel)^2 + (\mathcal{E}_{k_\parallel -} \pm \alpha_- k_\parallel)^2}, \quad e^{\pm i\theta} = \frac{k_\pm}{k_\parallel}. \tag{51}$$

3. *SO-induced effective-mass renormalization*

Expanding the energy dispersions [Eq. (48)] around $k_\parallel = 0$, we obtain to second order

$$\mathcal{E}_{k_\parallel \to 0,\lambda_1,\lambda_2} \approx \mathcal{E}_+ + \lambda_1 \mathcal{E}_- + \lambda_2(\alpha_+ + \lambda_1 \alpha_-)k_\parallel + \frac{\hbar^2 k_\parallel^2}{2m^*_{\lambda_1}}, \tag{52}$$

where $m^*_{\lambda_1}$ are the effective masses

$$m^*_\pm = \frac{m^*}{1 \pm \dfrac{2\mathcal{E}_{SO}}{\Delta\mathcal{E}}}, \tag{53}$$

where $\mathcal{E}_{SO} = \frac{1}{2} m^* \eta^2 / \hbar^2$ and $\Delta\mathcal{E} = 2\mathcal{E}_-$. Note that the mass renormalization is solely due to the intersubband-induced SO coupling η. For the realistic wells we investigate here $2\mathcal{E}_{SO}/\Delta\mathcal{E} \ll 1$ for single wells but can reach ~ 0.1 for double wells (Secs. IV and V).

4. *Determining the SO couplings*

As mentioned previously, we determine the SO orbit couplings (here specifically α_0, α_1, and η) from the self-consistent eigensolutions of the quantum well *without* spin orbit,[28] via Eqs. (40)–(43). In Sec. IV we detail the quantum-well systems investigated and briefly outline the self-consistent procedure used to obtain the eigensolutions (a full description is provided in Appendixes A and B). We then present results for single and double wells with two subbands; i.e., we calculate α_0, α_1, and η and discuss in detail the several distinct contributions to each of these quantities.

IV. QUANTUM-WELL SYSTEMS AND SELF-CONSISTENCY

Figure 2 shows a schematic view of the quantum-well system we study: a well of width L_w centered at $z=0$ (z: growth direction), and two adjacent symmetrically doped regions of widths w in the barriers. We also consider double wells by inserting an additional (central) barrier of width L_b in the well region. The doping densities of the left and right regions, ρ_a and ρ_b, respectively, can be used to control the degree of structural inversion asymmetry of the wells (in Sec. V, however, we present results only for $\rho_a = \rho_b$). The

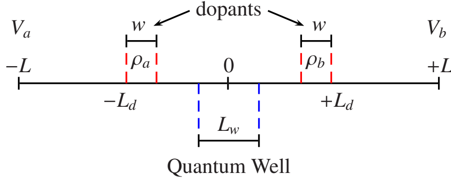

FIG. 2. (Color online) Schematic view of our quantum-well system. The doping densities ρ_a, ρ_b and the external gate voltages V_a and V_b can be used to control the degree of the structural inversion asymmetry.

external gates V_a and V_b, located at the end points $\pm L$, can also be used to control the degree of inversion asymmetry and to vary the areal electron density in the well.

Since our wells have many electrons and are subject to external gates, we have to solve the Schrödinger and Poisson equations self-consistently ("Hartree approximation"[31]) in order to determine their potential profile $V_{\mathrm{sc}}(z)$ [see Eq. (33)] and corresponding eigenfunctions and eigenenergies. In Appendixes A and B we describe in detail our standard self-consistent procedure.

Before going into the discussion of the SO couplings in detail, let us first have a look at the outcome of a typical self-consistent simulation we perform. Figure 3(a) shows the self-consistent potential V_{sc} (thick solid line) for a single well with two subbands; the corresponding self-consistent wave functions $\psi_0(z)$ and $\psi_1(z)$ are also shown. The energies of the two lowest subband edges (see levels in the well) are $\mathcal{E}_0 = 309.09$ meV and $\mathcal{E}_1 = 406.39$ meV ($\Delta\mathcal{E} = 97.3$ meV). Here we fix the chemical potential at $\mu = 413.40$ meV with respect to the $V=0$ origin ("constant chemical potential model," see below) and set the external gates to $V_a = 0$ and $V_b = 1200$ meV. The two subbands are occupied with areal densities $n_0 = 18.7422 \times 10^{11}$ cm^2 and $n_1 = 1.2578 \times 10^{11}$ cm^2, respectively. The electronic Hartree potential V_e (short dashed line) and the the external gates (plus modulation doping) contribution V_g (long dashed line) are also shown. Figure 3(b) shows the corresponding "force fields" $F_e = -dV_e/dz$ arising from the confined electrons in the well and $F_g = -dV_g/dz$ coming from the doping regions (± 12 nm to ± 18 nm) plus the external gates (F_g and F_e will be useful when discussing the SO couplings further below). Using the self-consistent solutions $\psi_\upsilon(z)$, $\upsilon = 0,1$, we can straightforwardly calculate the relevant SO couplings [via Eqs. (40)–(43)]: $\eta = -3.81$ meV nm, $\alpha_0 = -5.44$ meV nm, $\alpha_1 = -3.74$ meV nm, $\beta_0 = 0.87$ meV nm, and $\beta_1 = 2.50$ meV nm.

V. RESULTS

Here we focus on single and double quantum wells with only two subbands. More specifically, we calculate three SO couplings: the intersubband-induced SO coupling $\eta = \eta_{01}$ and the two Rashba-type couplings $\alpha_0 = \eta_{00}$ and $\alpha_1 = \eta_{11}$. We consider two experimentally relevant cases: the constant areal density (n_T-constant) and the constant chemical potential (μ-constant) models. In our simulations we always keep $V_a = 0$ as a reference potential and vary V_b; see Fig. 2. For completeness, we also calculate the two Dresselhaus constants β_0 and β_1 [see Eq. (44)] within each subband.

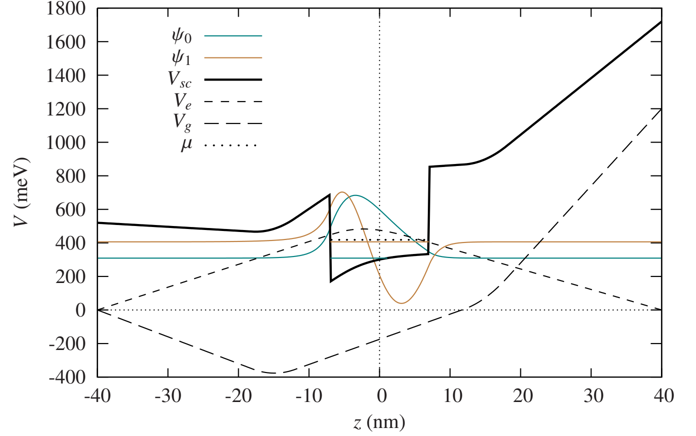

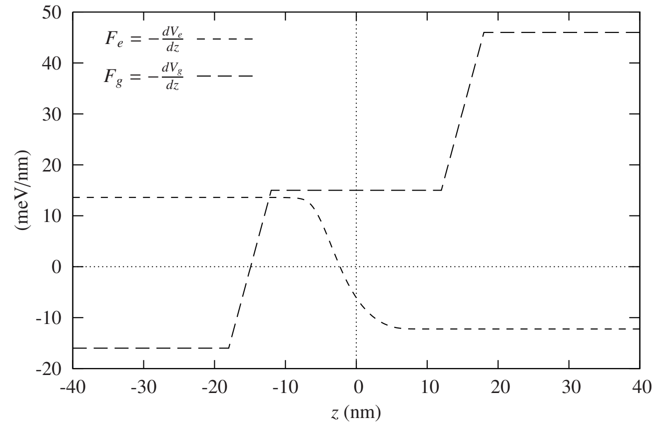

FIG. 3. (Color online) (a) Self-consistent potential energy V_{sc} (thick solid line) and the corresponding wave functions ψ_0 and ψ_1 for the single well $Al_{0.48}In_{0.52}As/Ga_{0.47}In_{0.53}As$ with external gates $V_a = 0$ eV and $V_b = 1.2$ eV (see Fig. 2). The electronic Hartree potential V_e (short dashed line), the external gate plus modulation doping contributions V_g (long dashed line), and the corresponding force fields $F_e = -dV_e/dz$ and $F_g = -dV_g/dz$ are also shown in (b). The two levels in the well (solid lines) denote the energies of the first and second subband edges, while the dotted level indicates the chemical potential.

A. Single wells

1. Single-well parameters

We consider a realistic $Al_{0.48}In_{0.52}As/Ga_{0.47}In_{0.53}As$ single quantum well.[32,33] We assume doping densities $\rho_a = \rho_b = 4 \times 10^{18}$ cm^{-3} with widths $w = 6$ nm ("sample 3" in Ref. 32). Table II summarizes band parameters, potential offsets,[25] well widths, and other important parameters of our system. The coefficients η_w and η_H in Table II are defined in Eq. (36) and Eq. (35), respectively. Here, the Dresselhaus parameter β_D in Eq. (44) is assumed to be the same as that of the GaAs (see Ref. 21).

TABLE II. Relevant parameters (Ref. 25) (see Fig. 1) (at 0.3 K) for the single quantum well $Al_{0.48}In_{0.52}As/Ga_{0.47}In_{0.53}As$ system in our simulations. The doping regions have widths $w=6$ nm and densities $\rho_a=\rho_b=4\times10^{18}$ cm^{-3} (see Fig. 2). All energies are in eV and lengths in nm; the coefficient η_H is in nm^2 and η_w in meV nm^2. The Dresselhaus coupling constant (Ref. 21) β_D is in meV nm^3.

$E_w=1.5296$	$\Delta_w=0.2998$	$w=6$	$E_P=25.3$
$E_g=0.8161$	$\Delta_g=0.3296$	$\delta_6=0.52$	$m^*/m_0=0.043$
$E_b=0$	$\Delta_b=0$	$\delta_{b6}=0$	$\epsilon_r=14.013$
$L=40$	$L_d=18$	$L_b=0$	$L_w=14$
$\eta_H=0.2376$	$\eta_w=0.0533$	$\eta_b=0$	$\beta_D=0.0237$

2. SO couplings: single wells

Figure 4 shows the strength of the Rashba (α_ν, $\nu=0,1$; dashed lines), Dresselhaus (β_ν, $\nu=0,1$; dotted lines) and intersubband-induced (η, solid line) SO couplings as functions of the gate voltage V_b, for both the n_T-constant and the μ-constant models, Figs. 4(a) and 4(b), respectively. At $V_b=V_a=0$ eV, our sample is completely symmetric and, as expected, the Rashba couplings α_0 and α_1 are zero. We note that the Dresselhaus couplings β_0 and β_1 are practically constant in both models. This follows from Eq. (45) which shows that in each subband the Dresselhaus coupling is essentially the difference between the expected value of the self-consistent potential in the respective subband and the corresponding eigenenergy. The Rashba couplings, on the other hand, vary considerably with V_b, although showing a similar trend in both models. Interestingly, they change signs about $V_b=0$ (symmetric configuration), but always with $|\alpha_0|>|\alpha_1|$. Our calculated α_0 within the μ-constant model [Fig. 4(b)] is consistent with the measurements of this quantity by Koga *et al.*,[32,33] whose samples have a constant chemical potential.

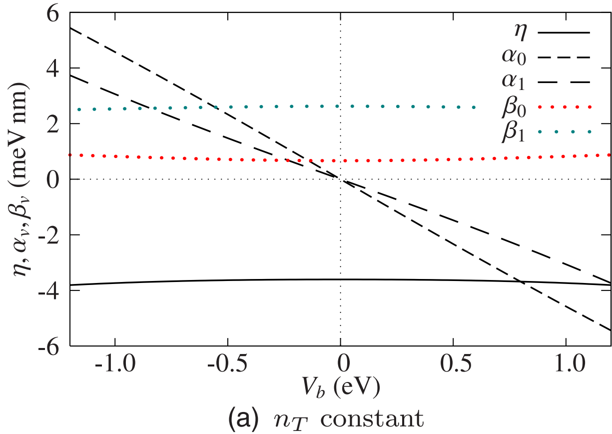

(a) n_T constant

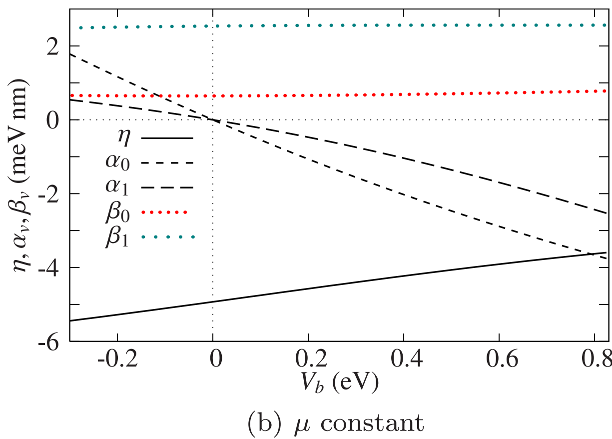

(b) μ constant

FIG. 4. (Color online) Rashba α, Dresselhaus β, and intersubband-induced η SO coupling constants for the $Al_{0.48}In_{0.52}As/Ga_{0.47}In_{0.53}As$ quantum well as functions of the gate voltage V_b (see Fig. 2). In (a) the total 2D electron density is kept constant at $n_T=20\times10^{11}$ cm^{-2} and in (b) the chemical potential is kept constant at $\mu=200$ meV.

The new intersubband-induced coupling η [see the solid lines in Figs. 4(a) and 4(b)] is nonzero even in the symmetric well configuration ($V_b=0=V_a$). It has a strength comparable to the Rashba and is at least twice as large as the Dresselhaus. In contrast to the Rashba couplings, the intersubband SO η does not change sign with V_b. In fact, for the single well investigated here η is almost constant with V_b, although it varies slightly more in the μ-constant model [compare the solid curves in Figs. 4(a) and 4(b)].

To more easily understand the results above, we analyze the several contributions to the SO couplings separately. To this end, we rewrite [see comments following Eq. (40)] $\eta_{\nu\nu'}$ for a single well in the form

$$\eta^{\mathrm{SW}}_{\nu\nu'} = \Gamma^{e}_{\nu\nu'} + \Gamma^{g}_{\nu\nu'} + \Gamma^{w}_{\nu\nu'}, \tag{54}$$

where we have set $\Gamma^{b}_{\nu\nu'}=0$ in Eq. (40), i.e., no central barrier contribution, and have split the Hartree contribution into its purely electronic $\Gamma^{e}_{\nu\nu'}$ and the external gate (plus doping potential) $\Gamma^{g}_{\nu\nu'}$ parts. Hence, for two subbands, each of the SO couplings has three contributions: $\eta=\eta^{\mathrm{SW}}_{01}=\Gamma^{e}_{01}+\Gamma^{g}_{01}+\Gamma^{w}_{01}$, $\alpha_0=\eta^{\mathrm{SW}}_{00}=\Gamma^{e}_{00}+\Gamma^{g}_{00}+\Gamma^{w}_{00}$, and $\alpha_1=\eta^{\mathrm{SW}}_{11}=\Gamma^{e}_{11}+\Gamma^{g}_{11}+\Gamma^{w}_{11}$. Figures 5(a)–5(c) show the above contributions separately for the n_T-constant case (similar results hold for the μ-constant model, in the parameter range studied).

Figure 5(a) shows that the external gates and doping contributions to η (Γ^{g}_{01} curve) are essentially zero, while the electronic Hartree contribution (Γ^{e}_{01} curve) and the structural (Γ^{w}_{01} curve) contributions are comparable in magnitude and both negative. In contrast, for both α_0 and α_1 the largest contributions come from the external gates together with doping regions [see the curve Γ^{g}_{00} in Fig. 5(b) and the curve Γ^{g}_{11} in Fig. 5(c)]; these account for 60% of α_0 and 100% of α_1. The electronic Hartree contribution is negligible in α_0 [curve Γ^{e}_{00} in Fig. 5(c)] while the structural part (Γ^{w}_{00}) accounts for about 30% of it. On the other hand, the structural and electronic Hartree contributions in α_1 essentially cancel out (same magnitude and opposite signs); cf. the Γ^{e}_{11} and Γ^{w}_{11} curves in Fig. 5(c).

We can understand the above remarks by looking at the self-consistent potentials and the "force fields" $F_e=-dV_e(z)/dz$ (short dashed curve) and $F_g=-dV_g(z)/dz$ (long dashed curve)—note that $\Gamma^{i}_{\nu\nu'}\sim\langle\nu|F_i|\nu\rangle$, $i\in\{e,g,w\}$,—in Fig. 3(b). This figure was obtained for $V_b=1.2$ eV, but it does display the general behavior for all quantities shown.

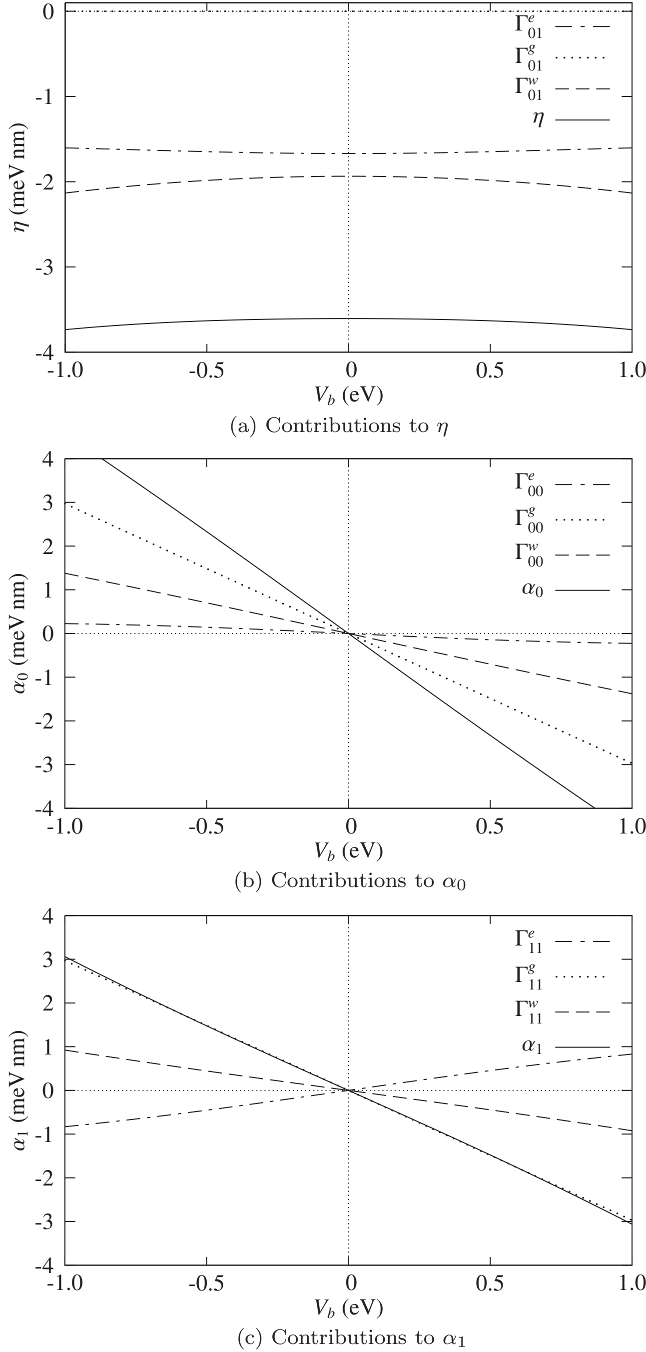

FIG. 5. Several distinct contributions to the coupling constants η (a), α_0 (b) and α_1 (c) for the single GaInAs quantum well shown in Fig. 4(a) (n_T-constant model) as functions of the external gate V_b (V_a=0). These contributions arise from the electron density (Hartree potential), the external gate (together with donor regions), and the structural well potential; these are denoted by the superscripts e, g and w, respectively.

The force field F_g is essentially constant, except within the donor regions where the wave functions are vanishingly small. Hence, the matrix element $\langle v|F_g|v\rangle$ [see Eqs. (40)–(43)] is approximately linear in the external gate V_b. This explains why the Rashba couplings α_v are strongly modulated by external gates. This is even more so for α_1, Fig. 5(c), for which the structural and electronic contributions cancel out. Looking at the wave functions ψ_0 and ψ_1 and the force field $F_e=-dV_e/dz$ in Fig. 3(b), we can see that the electronic Hartree contribution $(\sim-\langle v|F_e|v\rangle)$ is almost zero (though slightly negative) for the lowest subband and positive for the first subband. The structural well contributions Γ^w_{vv} [see Eq. (42)] to α_v are similar for both subbands, though $|\Gamma^w_{00}|\geq|\Gamma^w_{11}|$, because the nonzero biases ($V_b\neq 0$) cause the wave functions to shift toward one side of the well [e.g., V_b=1.2 eV in Fig. 3(a)].

On the other hand, the contribution $\Gamma^g_{01}\sim-\langle 0|F_g|1\rangle$ to the intersubband coupling η is essentially zero since the wave functions [ψ_0 and ψ_1 in Fig. 3(a)] are orthogonal and, again, F_g is constant. Hence η is not as sensitive to the external gates as the Rashba couplings. Most of the modulation of η arises from the electronic Hartree and structural contributions, which both have the same sign and magnitude as shown in Fig. 5(a).

TABLE III. Relevant parameters (Refs. 21 and 25) (at 1 K) for the InSb double well (see Figs. 1 and 2). The width of the doping regions is w=4 nm and their densities are $\rho_a=\rho_b=3\times10^{18}$ cm^{-3}. All energies are in eV and lengths in nm. The coefficient η_H is measured in nm^2 while η_w and η_b are measured in meV nm^2. The Dresselhaus constant β_D is measured in meV nm^3. The parameters in the last column are to the InSb binary compound.

E_w=0.9922	Δ_w=0.6964	w=4	E_P=23.3
E_g=0.2350	Δ_g=0.8100	δ_6=0.6133	m^*/m_0=0.0135
E_b=0.4477	Δ_b=0.7675	δ_{b6}=0.1723	ϵ_r=16.8
L=100	L_d=65	L_b=20	L_w=50
η_H=0.2171	η_w=0.7627	η_b=5.0873	β_D=0.326

B. Double well

1. Double-well parameters

Table III shows the band parameters[21,25] for the double quantum well $Al_{0.4}In_{0.6}Sb/InSb$ with one central barrier $InSb/Al_{0.12}In_{0.88}Sb$. Hereafter we refer to this heterostructure as InSb double well. The meaning of some of these parameters (e.g., band offsets) can be seen in Figs. 1 and 2.

2. SO couplings: double-well case

Figure 6 shows the Rashba α, Dresselhaus β, and intersubband-induced η SO couplings as functions of the gate voltage V_b (here again V_a=0) for both the n_T-constant (a) and μ-constant (b) models. We first discuss the n_T-constant model [Fig. 6(a)]. Here the Rashba couplings (dashed lines) are most sensitive to the external bias V_b, being essentially the largest of all SO couplings for very asymmetric structures (i.e., high biases). The Dresselhaus couplings (dotted lines) are almost identical ($\beta_0\approx\beta_1$) and mostly independent of the external gates. The SO coupling η (solid line) is an even function of the external gate V_b and presents a "resonant behavior" around the $V_b=V_a=0$ eV configuration, at which our sample is symmetric. While the Rashba couplings are both zero at this symmetric configuration, we note that they are odd functions of the external gate

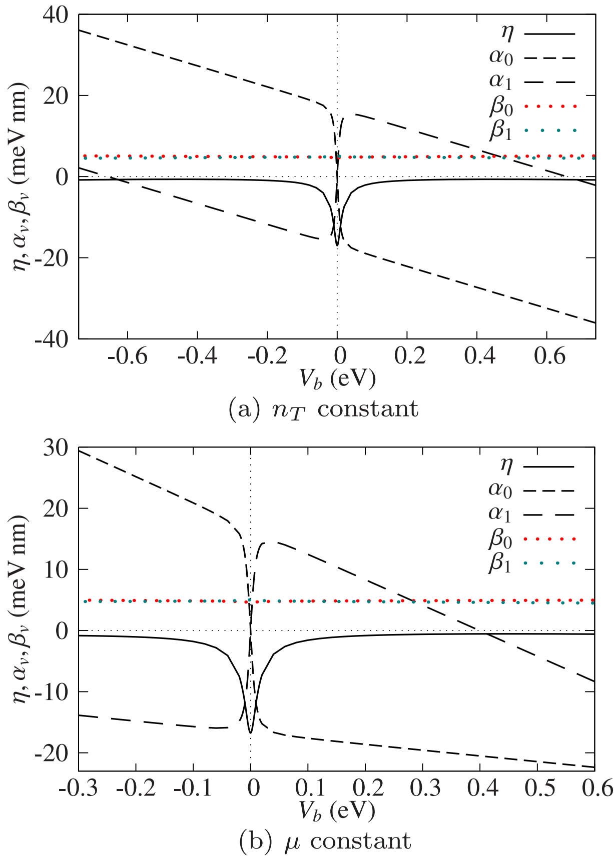

FIG. 6. (Color online) Rashba α, Dresselhaus β, and the intersubband-induced η SO couplings for a InSb double quantum well as functions of the right gate voltage V_b. In (a) the total electron density is kept constant at $n_T=10\times10^{11}$ cm^{-2} and in (b) the chemical potential is kept constant at $\mu=100$ meV (relative to initial bottom well).

(with $|\alpha_0|>|\alpha_1|$), have opposite signs, and abruptly change magnitudes around $V_b=0$ (over a 40 meV wide region). For the μ-constant model [Fig. 6(b)], a similar picture as above also holds; note, however, that in contrast to the n_T-constant model, in the μ-constant case the positive and negative bias configurations are not equivalent as they correspond to the well having different numbers of electrons.

For completeness we show in Fig. 7 the behavior of all coupling constants near the symmetric point $V_b=V_a=0$ eV for the double well in Fig. 6(a). Note that the Dresselhaus couplings β_0 and β_1 present a (double) crossing over a 160 meV wide region; see Fig. 7(b) (however, this is a minor effect: note the change in the scale of the vertical axis). While the resonant behavior of η is accompanied by an enhancement of about 10 in its magnitude [see Fig. 6(a)], we see no substantial change in the magnitudes of the β's near the zero-bias case [cf. Figs. 7(a) and 7(b)].

The relative strengths of the Rashba and Dresselhaus coupling constants to the intersubband-induced SO coupling are shown in Fig. 8. The Rashba couplings have the largest strengths (note the prefactors in front of α_v/η in the legends). In contrast to β_v/η, the linear behavior of the Rashba ratios α_v/η near $V_b=0$ (see insets) shows that α_v and η undergo similar variations near the symmetric configuration. As observed before, the intersubband-induced coupling η becomes important near $V_b=0$ (Fig. 6).

Figure 9 (similar to Fig. 5 for the single-well case) shows the several contributions to each of the SO couplings η, α_0, and α_1 for the double-well case. Here, in addition to the electronic Hartree, the gate (+ doping regions), and the well contributions, there is an additional structural term arising from the central barrier (superscript b). A general feature in Figs. 9(a)–9(c) is that the structural contributions (well and central barrier) almost cancel out because they have opposite signs (see the curves with superscripts w and b). These terms have opposite signs because the derivatives $dh_w(z)/dz$ (well) and $dh_b(z)/dz$ (barrier), which enter the coupling constants [see Eqs. (40), (42), and (43)], have opposite slopes. Similarly to the single-well case [Fig. 5(a)] the contribution of the external gates (which includes the doping regions) to the intersubband SO coupling η is vanishingly small [see the Γ_{01}^g curve in Fig. 9(a)]. Hence, η is mostly due to the electronic Hartree contribution [curve Γ_{01}^e in Fig. 9(a)]. In addition, the gate contribution to α_0 and α_1 for the InSb double well is linear in V_b as for the single-well case. Hence, the Rashba couplings α_0 and α_1 for the double InSb well are essentially

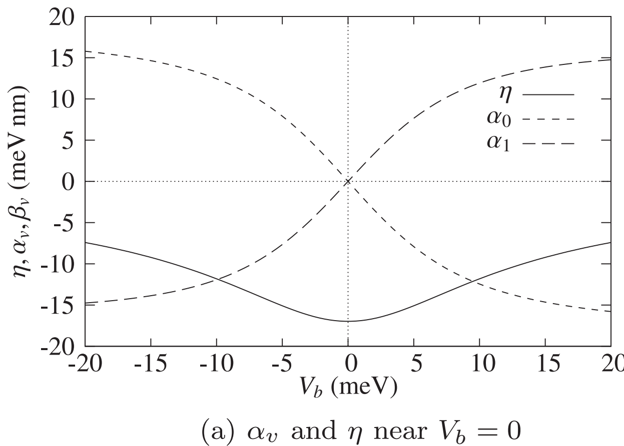

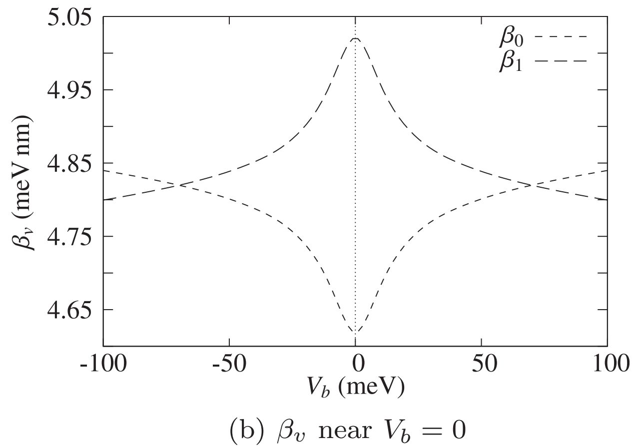

FIG. 7. Rashba α, intersubband-induced η, and Dresselhaus β couplings vs V_b about the symmetric configuration $V_b=V_a=0$ eV for the double InSb well in Fig. 6(a).

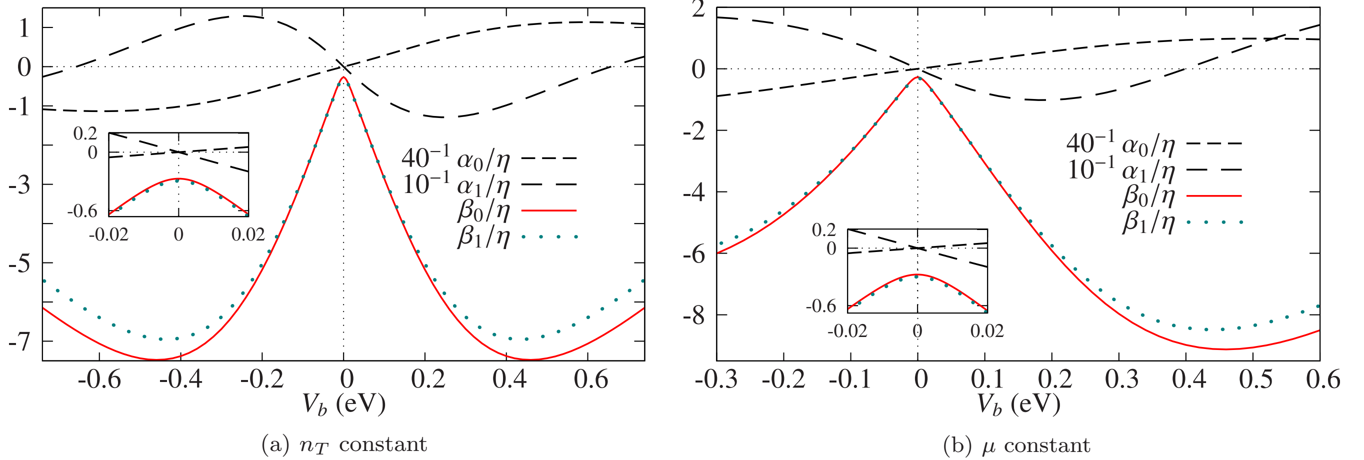

FIG. 8. (Color online) Ratios α_v/η and β_v/η for the InSb double well in Fig. 6. The insets are blowups around $V_b=0$, the symmetric configuration.

determined by the electronic (Hartree) contribution and are modulated by the gate contribution. Summarizing: looking at Fig. 9, we can see that (i) the structural contributions (well and barrier; dashed curves) almost cancel out, and (ii) the external gate (dotted curves) modulates the Rashba couplings α_v; therefore, for the double well investigated here (iii) most of the strength of these three coupling constants (η, α_0, and α_1) comes from the electronic contribution (dot-dashed curves).

It is instructive to investigate in more detail how the resonant behavior in η comes about, as well as the abrupt changes in the Rashba couplings; see Fig. 6. This can be accomplished by looking more closely at the self-consistent wave functions of the InSb double well around the symmetric configuration ($V_b=0$). The top row in Fig. 10 shows the self-consistent potential profile of the double well and the normalized wave functions ψ_0 (short dashed line) and ψ_1 (long dashed line) for the lowest $v=0$ and for the first excited $v=1$ subbands at three distinct gate voltages: $V_b=+0.3$ eV, $V_b=0$ eV, and $V_b=-0.3$ eV (left, center, and right columns, respectively). For positive bias ψ_0 is mostly localized in the left well and ψ_1 in the right well, while for negative biases this configuration is reversed. The electronic Hartree contribution to the potential energy V_e and the corresponding force field $F_e=-dV_e/dz$ are shown on the second row, thin and thick lines, respectively. Notice that F_e is practically zero in the central barrier region ($-10\leq z\leq 10$ nm) and has opposite signs within the wells ($-25\leq z\leq -10$ nm and $10\leq z\leq 25$ nm). Hence the quantities $F_e^{00}(z)=\psi_0(z)F_e\psi_0(z)$, $F_e^{11}(z)=\psi_1(z)F_e\psi_1(z)$, and $F_e^{01}(z)=\psi_0(z)F_e\psi_1(z)$ have the forms shown on the third and fourth rows. The integral over z of these quantities defines the electronic Hartree contributions to the spin-orbit couplings α_0, α_1, and η, i.e., $\Gamma_{00}^e \sim \langle 0|F_e|0\rangle$, $\Gamma_{11}^e \sim \langle 1|F_e|1\rangle$, and $\Gamma_{01}^e \sim \langle 0|F_e|1\rangle$, respectively. Since the electronic Hartree contributions dominate over the others, see Figs. 9(a)–9(c), the abrupt changes in the Rashba couplings and the resonant behavior of η around $V_b=0$ follow straightforwardly.

3. Density anticrossings and effective masses

Figures 11(a) and 11(b) show anticrossings of the areal densities n_T for the InSb double well near the symmetric configuration $V_b=0$,[34] where the strength of the intersubband-induced SO coupling η is the strongest (-16.7482 meV nm) while the the energy difference between the subband edges $\Delta\mathcal{E}=\mathcal{E}_1-\mathcal{E}_0$ (0.9353 meV) is the smallest. In accord with Eq. (52), we find an appreciable change in the bulk effective mass m^* near $k_\parallel=0$.[35] The ratio $\mathcal{E}_{SO}/\Delta\mathcal{E}$ [see Eq. (53)] is shown in Fig. 11(c) and the ratio $\bar{m}_\pm=m_\pm^*/m^*$ in Fig. 11(d). These intersubband-SO-induced changes in the effective masses $m_\pm^*$ may have a sizable effect on the measured mobilities and cyclotron frequencies in InSb wells.

VI. SUMMARY

Starting from the 8×8 Kane model in heterostructures, we have derived in some detail an effective electron Hamiltonian which contains a new intersubband-induced SO interaction term which arises in quantum wells with more than one quantized subband. Unlike the usual Rashba SO term, the intersubband SO coupling here is nonzero even for symmetric wells. For structurally asymmetric wells we have also accounted for the Rashba-type SO interaction within each subband.

We have also outlined the projection procedure (“folding down”) to obtain quasi-2D Hamiltonians by integrating out the confined variables. For two subbands in asymmetric wells we find a 4×4 quasi-2D Hamiltonian resembling Rashba’s, but containing three SO couplings: the two Rashba couplings α_0 and α_1 and the intersubband SO coupling η. For this two-subband case, we have investigated thoroughly these three SO couplings for realistic modulation-doped single and double wells. By performing a detailed self-consistent calculation in which we solve both Poisson’s and Schrödinger’s equation iteratively, we have determined the strengths of α_0, α_1, and η.

Each of these coupling strengths contains contributions arising from (i) the potential-well (and barrier) offsets, (ii) the electronic Hartree potential, and (iii) the external gate potential plus the modulation doping potential. We have performed our simulations by either keeping the areal electron

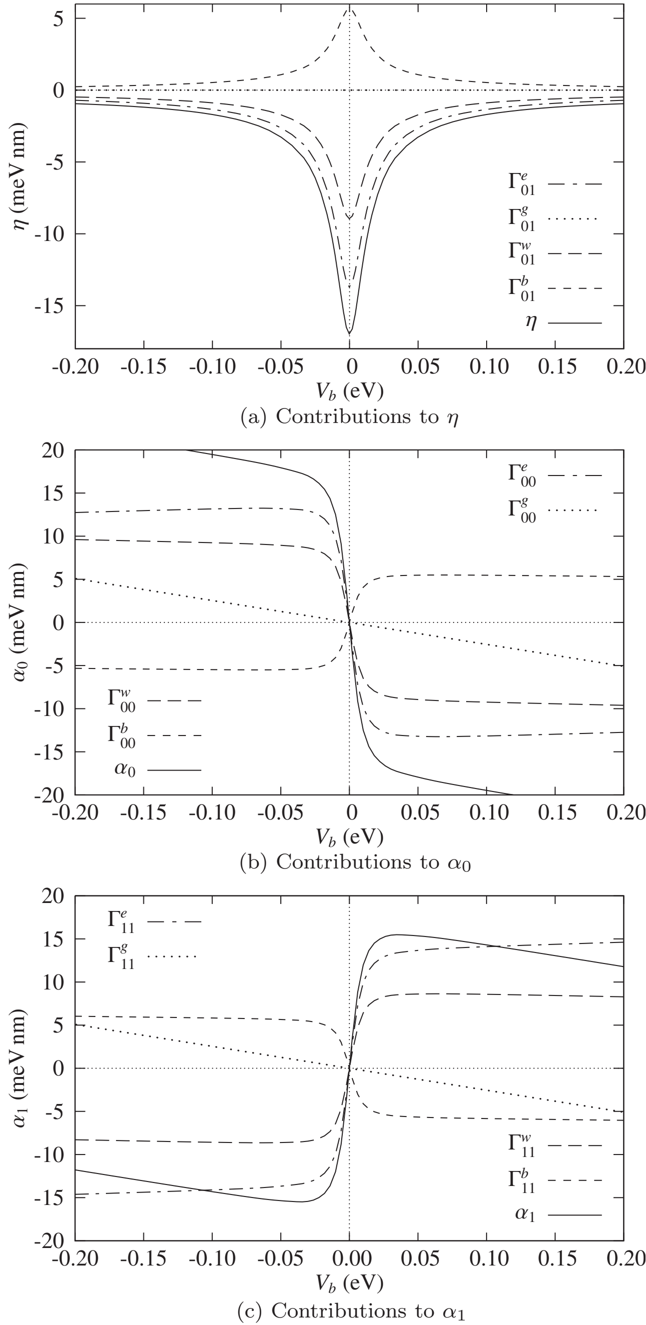

FIG. 9. Different contributions to the SO couplings η, α_0, and α_1 for the InSb double well in the constant areal density model [see Fig. 6(a)] as functions of the external gate V_b (V_a=0). In the subfigures we show the contributions to the coupling constants coming from the areal electronic density, indicated by the superscript e, and from the external gate+donor regions g, and also from the structural potential, being w for the well and b for the central barrier.

density n_T in the well fixed (n_T-constant model) or by keeping the chemical potential μ fixed (μ-constant model). In the parameter range investigated, both models give similar result for the calculated SO couplings.

For the single well investigated, α_0 is mostly determined by the external gate (+ modulation doping) contribution, with the structural+electronic Hartree being about half of that of the gate. On the other hand, α_1 is essentially determined by the external gate (+ modulation doping) contribution, since the electronic Hartree and the structural contributions cancel out. The intersubband SO coupling η is essentially determined by the electronic Hartree potential and

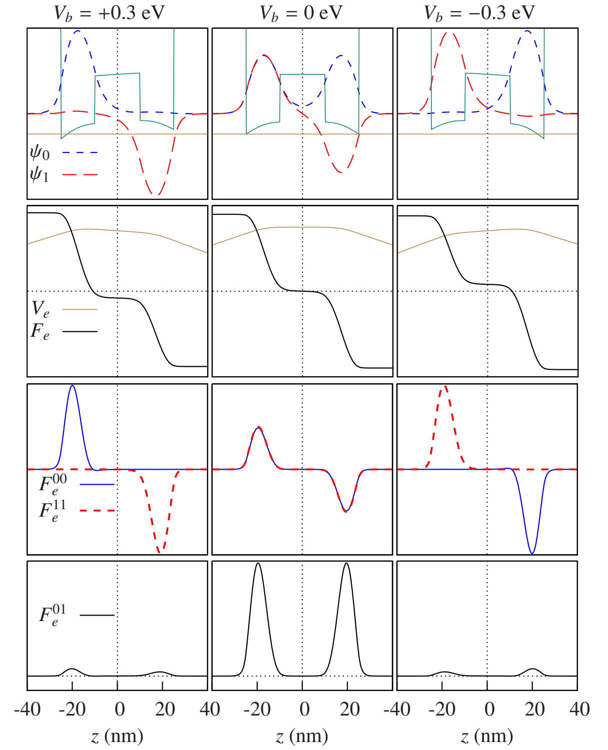

FIG. 10. (Color online) Top row: Wave functions ψ_0 and ψ_1 for the InSb double well (Sec. V B 1) with external biases V_b= +0.3 eV, V_b=0 eV, and V_b=−0.3 eV (first, second, and third columns, respectively). The electronic Hartree contribution $V_e(z)$ to the potential energy and the corresponding force field F_e=$-dV_e/dz$ are shown on the second row. The third row shows the quantities $F_e^{00}(z)=\psi_0 F_e \psi_0$ and $F_e^{11}(z)=\psi_1 F_e \psi_1$ and the bottom row shows $F_e^{01}(z)=\psi_0 F_e \psi_1$. Here n_T=10×10^{11} cm^{-2}. The vertical dotted lines mark the center of the 20-nm-wide AlInSb barrier within the 50-nm-wide InSb well.

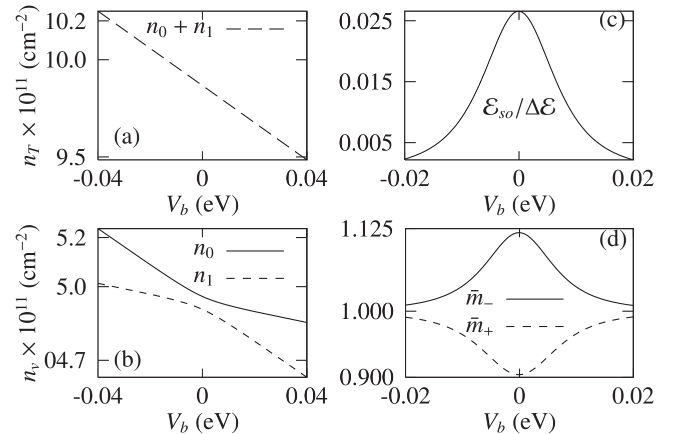

FIG. 11. (a) Total electronic areal density n_T=n_0+n_1, (b) subband areal densities n_0 and n_1, (c) ratio $\mathcal{E}_{SO}/\Delta\mathcal{E}$ and (d) effective-mass ratios $\bar{m}_\pm$=$m^*_\pm/m^*$ [Eq. (53)], as functions of the external gate V_b (V_a=0) in the μ-constant model (μ=100 meV).

the structural potential contributions (both of the same order); the external gate (+ modulation doping) potential contribution to η is nearly zero. Hence, while α_0 and α_1 can be modulated by the external gate potential, η is only slightly influenced by it.

For double wells the SO couplings show more peculiar behaviors. While the Rashba couplings α_0 and α_1 abruptly change magnitudes and signs around the symmetric configuration (zero external bias), the intersubband-induced SO coupling presents a resonant behavior being enhanced by a factor of 10 (with no sign change) around this point. For the double well investigated the structural contributions to α_0, α_1 and η, due to the potential offsets of the edges of the well and the central barrier, cancel out. In addition, the contribution of the external gate (+ doping region) to η is vanishingly small (as for the single-well case). Interestingly, the dominant contribution to all three SO couplings α_0, α_1, and η comes from the electronic Hartree potential. However, this contribution is highly influenced by the external gate, particularly around the symmetric configuration as the electrons can easily localize in either well for slight (positive or negative) changes in the gate.

Finally, we have also calculated the effective-mass renormalization due to the intersubband SO interaction (the Rashba-type interaction does not produce a mass change). For the double well investigated, we find that this mass renormalization is the largest ($\sim 10\%$) around the symmetric potential configuration (zero external bias), for which the splitting of the two subbands is the smallest. This mass change can possibly have an effect on mobility and cyclotron-resonance measurements.

ACKNOWLEDGMENTS

We thank G. J. Ferreira, H. J. P. Freire, and L. Viveiros for useful discussions. This work was supported by the Swiss NSF, the NCCR Nanoscience, JST ICORP, CNPq and FAPESP.

APPENDIX A: SELF-CONSISTENT PROCEDURE

1. Effective Schrödinger equation

The single-particle electron Hamiltonian H_{QW} of our quantum wells [Eq. (31)] is clearly separable. The transverse motion (x,y) is free while that along the z direction is confined by the quantum well. To solve the corresponding Schrödinger equation $H_{\mathrm{QW}}\Psi_{\mathbf{k}_\parallel v}(\mathbf{r})=E_{\mathbf{k}_\parallel v}\Psi_{\mathbf{k}_\parallel v}(\mathbf{r})$ we assume a wave function of the form

$$\Psi_{\mathbf{k}_\parallel v}(\mathbf{r}) = \langle \mathbf{r}|\mathbf{k}_\parallel v\rangle = \frac{1}{\sqrt{A}}\exp(i\mathbf{k}_\parallel\cdot\mathbf{r}_\parallel)\psi_v(z), \tag{A1}$$

(A is a normalizing area) which leads to the 1D Schrödinger equation

$$\left(-\frac{\hbar^2}{2m}\frac{d^2}{dz^2}+V_{\mathrm{sc}}(z)\right)\psi_v(z) = \left(E_{\mathbf{k}_\parallel v}-\frac{\hbar^2k_\parallel^2}{2m^*}\right)=\mathcal{E}_v\psi_v(z), \tag{A2}$$

from which we obtain the quantized energy levels $\mathcal{E}_v$ and wave functions $\psi_v(z)$. As we shall see, the subband structure of the well $E_{\mathbf{k}_\parallel v}=\mathcal{E}_v+\hbar^2k_\parallel^2/2m^*$ and the corresponding total wave function $\Psi_{\mathbf{k}_\parallel v}(\mathbf{r})$ will be used (within a self-consistent procedure) to construct the electron charge density, from which the corresponding Hartree potential can be obtained via the Poisson equation.

As mentioned in Sec. III B V_{sc} in Eq. (A2) contains not only the structural confining potential but also the "Hartree contributions:" (i) the purely electronic mean-field potential (electronic Hartree potential) and (ii) the external gate potential plus the modulation doping potential. Further down we discuss these contributions in detail. Each of these contributions is determined from a Poisson equation with an appropriate charge distribution and boundary condition.

a. Self-consistency

Since the electronic charge distribution $\rho_e(z)$ ($\propto\Sigma_v|\langle \mathbf{r}|\mathbf{k}_\parallel v\rangle|^2$) depends on the detailed form of the several potentials (modulation doping, gates, and electronic Hartree), and these, in turn, depend on $\rho_e(z)$, we have to solve the problem self-consistently. The standard procedure is as follows: (i) to solve Eq. (A2) with an initial guess for V_{sc} which we take to be just the structural potential plus the external gates and modulation doping potential [i.e., in the first run we do not include the electronic Hartree potential $V_e(z)$]; (ii) to construct the electronic charge density $\rho_e(z)$ [from the eigenfunctions obtained in step (i)] and the corresponding $V_e(z)$ via Poisson equation; and (iii) to solve again the Schrödinger equation with the new V_{sc}, which in this new iteration includes $V_e(z)$ (as well as the other potentials: gates, modulation doping, and structural confinement). We repeat this process until convergence is attained.

b. Numerics

We use the sixth-order Numerov method to solve the Schrödinger equation.[36–39] Poisson equation (see Appendix A 2) is solved via a semianalytical Numerov method.[40] All numerical integrations are performed using a Gaussian integration method.[41] In our numerical implementation we use the dimensionless form of Eq. (A2),

$$\frac{d^2\tilde{\psi}_v}{d\tilde{z}^2}=\tilde{V}_v\tilde{\psi}_v,\quad \tilde{\psi}_v=\psi_v(\tilde{z}),\quad \tilde{z}=\frac{z}{l}, \tag{A3}$$

where

$$\tilde{V}_v=\frac{2\pi}{\varepsilon_1}[V_{\mathrm{sc}}(\tilde{z})-\mathcal{E}_v],\quad \varepsilon_1=\frac{\pi\hbar^2}{m^*l^2}. \tag{A4}$$

We choose $l=1$ nm as our length unit and ε_1 as the relevant energy scale.

2. Poisson equations for the electronic and gate plus modulation doping potentials

The self-consistent electronic potential energy $V_{\mathrm{sc}}(z)=-e\phi_{\mathrm{sc}}(z)$ can be split in two parts, $V_{\mathrm{sc}}(z)=V_{wb}(z)+V_H(z)$. $V_{wb}(z)=V_w(z)+V_b(z)$ described the structural quantum-well potential. The "Hartree" contribution $V_H(z)=V_e(z)+V_g(z)$ arises from the electronic charge density and from the exter-

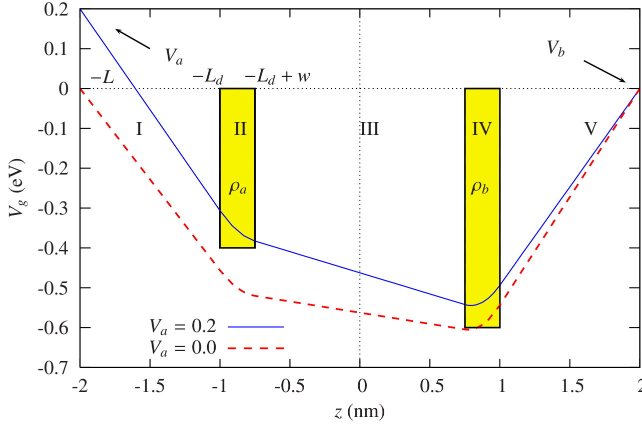

FIG. 12. (Color online) Schematic representation of doping layers of width w and densities ρ_a and ρ_b plus the external gates V_a and V_b. By varying the external gates (we usually keep $V_a=0$ and vary V_b) we can alter the spatial symmetry of our quantum wells; see Fig. 2. The curves illustrate the calculated gate+modulation doping potential $V_g(z)$ for $V_a=V_b$ (dashed line) and $V_a>V_b$ (solid line), both with $\rho_a>\rho_b$.

nal gates plus the modulation doping regions (symmetrically located around the well; see Fig. 12). Figure 12 also shows the Dirichlet boundary conditions V_a and V_b, which are in fact the external gates at the end points $\pm L$ of our system.

a. Gate+modulation doping potential

We can write separate Poisson equations for $V_g(z)$ and $V_e(z)$ as these arise from distinct charge densities. For $V_g(z)$ we have (see Fig. 12)

$$\frac{d^2}{dz^2}V_g=\frac{e^2}{\epsilon_r\epsilon_0}\begin{cases}0, & \text{(I)}:-L\le z\le -L_d,\\ \rho_a, & \text{(II)}:-L_d\le z\le -L_d+w,\\ 0, & \text{(III)}:-L_d+w\le z\le L_d-w,\\ \rho_b, & \text{(IV)}:L_d-w\le z\le L_d,\\ 0, & \text{(V)}:L_d\le z\le L,\end{cases} \tag{A5}$$

where ϵ_0 is the permittivity, ϵ_r is the dielectric constant,[42,43] and $\rho_{a,b}$ are the doping densities. From the continuity of $V_g(z)$ and its first derivative and assuming the Dirichlet boundary conditions $V_g(-L)=V_a$ and $V_g(+L)=V_b$, we find

$$V_g=\begin{cases}c_1z+c_2, & \text{(I)}:-L\le z\le -L_d,\\ \frac{1}{2}Az^2+c_3z+c_4, & \text{(II)}:-L_d\le z\le -L_d+w,\\ c_5z+c_6, & \text{(III)}:-L_d+w\le z\le L_d-w,\\ \frac{1}{2}Bz^2+c_7z+c_8, & \text{(IV)}:L_d-w\le z\le L_d,\\ c_9z+c_{10}, & \text{(V)}:L_d\le z\le L,\end{cases} \tag{A6}$$

with

$$A=\frac{e^2\rho_a}{\epsilon_r\epsilon_0},\quad B=\frac{e^2\rho_b}{\epsilon_r\epsilon_0}, \tag{A7}$$

where the constants c_i are given in Appendix B. Figure 12 shows two solutions of Eq. (A5), both having $\rho_a>\rho_b$ and $V_a=V_b$ (dashed line) and $V_a>V_b$.

b. Electronic Hartree potential

The electronic Hartree contribution $V_e(z)$ is determined from

$$\frac{d^2}{dz^2}V_e(z)=-\frac{e}{\epsilon_r\epsilon_0}\rho_e(z), \tag{A8}$$

with (including spin)

$$\rho_e(z)=\frac{2e}{A}\sum_{v,k_\parallel}|\psi_v(z)|^2f(E_{k_\parallel v})=\frac{em^*}{\pi\hbar^2}k_BT\lambda_e(z), \tag{A9}$$

where

$$\lambda_e(z)=\sum_v|\psi_v(z)|^2\ln[1+e^{\beta(\mu-\mathcal{E}_v)/k_BT}], \tag{A10}$$

and

$$f(E_{k_\parallel v})=\frac{1}{1+e^{(E_{k_\parallel v}-\mu)/k_BT}},\quad E_{k_\parallel v}=\frac{\hbar^2k_\parallel^2}{2m^*}+\mathcal{E}_v. \tag{A11}$$

We solve Eq. (A8) for $V_e(z)$ using an accurate Numerov scheme[40] with the Dirichlet boundary conditions $V_e(\pm L)=0$. Similarly to the Schrödinger equation in Eq. (A3), we find it convenient here to write the Poisson Eq. (A8) in a dimensionless form

$$\frac{d^2}{d\tilde{z}^2}\tilde{V}_e=-\tilde{\lambda}_e,\quad \tilde{\lambda}_e=\frac{k_BT}{\varepsilon_1}l\lambda_e(\tilde{z}),\quad \varepsilon_2\tilde{V}_e=V_e(\tilde{z}), \tag{A12}$$

where ε_1 is the energy scale given in Eq. (A4) and

$$\varepsilon_2=\frac{e^2}{\epsilon_r\epsilon_0 l}. \tag{A13}$$

c. Electron density and chemical potential

From the total electronic charge

$$\int dV\rho_e(z)=en_TA, \tag{A14}$$

we can straightforwardly [using Eq. (A9)] obtain the total areal concentration of electrons

$$n_T=\sum_v n_v, \tag{A15}$$

with the n_v's denoting the subband occupations

$$n_v=\frac{m^*}{\pi\hbar^2}k_BT\ln[1+e^{(\mu-\mathcal{E}_v)/k_BT}]. \tag{A16}$$

When n_T is fixed (i.e., the n_T-constant model), we can determine the chemical potential μ from Eq. (A15),

$$\frac{\pi\hbar^2 n_T}{m^* k_B T} = \sum_v \ln[1 + e^{(\mu-\mathcal{E}_v)/k_B T}]. \tag{A17}$$

APPENDIX B: COEFFICIENTS c_i's

Using the continuity of V_g and its first derivative together with the (Dirichlet) boundary conditions at the end points $V_g(-L)=V_a$ and $V_g(L)=V_b$, we can determine the coefficients c_i's appearing in Eq. (A6). In the regions I and V we find

$$c_1 = -\frac{2L_d - w}{2L} wC_- - wC_+ - \frac{V_-}{L}, \tag{B1}$$

$$c_2 = -\frac{1}{2}(2L_d - w)wC_- - LwC_+ + V_+, \tag{B2}$$

$$c_9 = -\frac{2L_d - w}{2L} wC_- + wC_+ - \frac{V_-}{L}, \tag{B3}$$

$$c_{10} = +\frac{1}{2}(2L_d - w)wC_- - LwC_+ + V_+, \tag{B4}$$

with

$$C_\pm = \frac{1}{2}(A \pm B), \quad V_\pm = \frac{1}{2}(V_a \pm V_b), \tag{B5}$$

and A and B defined in Eq. (A7). In the modulation doping regions II and IV, we have

$$c_3 = \frac{w^2 - 2wL_d + 2LL_d}{2L} C_- + (L_d - w)C_+ - \frac{V_-}{L}, \tag{B6}$$

$$c_4 = +\frac{1}{2}(L_d - w)^2 C_- + \frac{1}{2}(L_d^2 - 2wL)C_+ + V_+, \tag{B7}$$

$$c_7 = \frac{w^2 - 2wL_d + 2LL_d}{2L} C_- - (L_d - w)C_+ - \frac{V_-}{L}, \tag{B8}$$

$$c_8 = -\frac{1}{2}(L_d - w)^2 C_- + \frac{1}{2}(L_d^2 - 2wL)C_+ + V_+. \tag{B9}$$

In the central region III, we have

$$c_5 = +\frac{2L - 2L_d + w}{2L} wC_- - \frac{V_-}{L}, \tag{B10}$$

$$c_6 = -\frac{1}{2}(2L - 2L_d + w)wC_+ + V_+. \tag{B11}$$

*sousa@if.sc.usp.br
†egues@if.sc.usp.br

[1] S. Datta and B. Das, Appl. Phys. Lett. **56**, 665 (1990); see also J. C. Egues, G. Burkard, and D. Loss, *ibid.* **82**, 2658 (2003), for a spin FET proposal with additional spin control due to spin-orbit induced interband coupling.

[2] E. I. Rashba, Sov. Phys. Solid State **2**, 1109 (1960).

[3] Y. A. Bychkov and E. I. Rashba, J. Phys. C **17**, 6039 (1984).

[4] Y. A. Bychkov and E. I. Rashba, JETP Lett. **39**, 78 (1984).

[5] G. Engels, J. Lange, T. Schäpers, and H. Lüth, Phys. Rev. B **55**, R1958 (1997).

[6] J. Nitta, T. Akazaki, H. Takayanagi, and T. Enoki, Phys. Rev. Lett. **78**, 1335 (1997).

[7] G. Dresselhaus, Phys. Rev. **100**, 580 (1955).

[8] S. A. Wolf, D. D. Awschalom, R. A. Buhrman, J. M. Daughton, S. von Molnár, M. L. Roukes, A. Y. Chtchelkanova, and D. M. Treger, Science **294**, 1488 (2001).

[9] *Semiconductor Spintronics and Quantum Computation*, edited by D. Awschalom, D. Loss, and N. Samarth (Springer, New York, 2002).

[10] I. Žutić, J. Fabian, and S. D. Sarma, Rev. Mod. Phys. **76**, 323 (2004).

[11] J. Schliemann, D. Loss, and R. M. Westervelt, Phys. Rev. Lett. **94**, 206801 (2005).

[12] J. Schliemann, D. Loss, and R. M. Westervelt, Phys. Rev. B **73**, 085323 (2006).

[13] J. Schliemann, J. Carlos Egues, and D. Loss, Phys. Rev. Lett. **90**, 146801 (2003).

[14] B. A. Bernevig, J. Orenstein, and S. C. Zhang, Phys. Rev. Lett. **97**, 236601 (2006).

[15] E. Bernardes, J. Schliemann, M. Lee, J. C. Egues, and D. Loss, Phys. Rev. Lett. **99**, 076603 (2007).

[16] J. J. Krich and B. I. Halperin, Phys. Rev. Lett. **98**, 226802 (2007).

[17] E. Bernardes, J. Schliemann, J. C. Egues, and D. Loss, Phys. Status Solidi C **3**, 4330 (2006).

[18] E. O. Kane, J. Phys. Chem. Solids **1**, 249 (1957).

[19] G. Bastard, *Wave Mechanics Applied to Semiconductor Heterostructures* (Halsted, Les Ulis, France, 1988).

[20] R. Winkler, *Spin-Orbit Coupling Effects in Two-Dimensional Electron and Hole Systems*, Springer Tracts in Modern Physics Vol. 191 (Springer, New York, 2003).

[21] J. M. Jancu, R. Scholz, E. A. de Andrada e Silva, and G. C. La Rocca, Phys. Rev. B **72**, 193201 (2005).

[22] D. M. Wood and A. Zunger, Phys. Rev. B **53**, 7949 (1996).

[23] E. L. Ivchenko and G. E. Pikus, *Superlattices and Other Heterostructures*, Springer Series in Solid-State Sciences Vol. 110 (Springer, New York, 1997).

[24] T. Darnhofer and U. Rössler, Phys. Rev. B **47**, 16020 (1993).

[25] I. Vurgaftman, J. R. Meyer, and L. R. Ram-Mohan, J. Appl. Phys. **89**, 5815 (2001).

[26] The renormalization of the conduction wave function is crucial to obtain an effective Pauli-type equation which properly includes the Darwin term and other higher-order corrections. Winkler discusses this point in detail in Ref. 20 (chapters 5 and 6).

[27] Here we neglect the Darwin and all higher-order terms and focus on only the Rashba-type contributions.

[28] Here we are following a procedure similar to that used by W.

Zawadzki and P. Pfeffer, Semicond. Sci. Technol. **19**, R1 (2004), that is, we neglect the spin-dependent boundary conditions along the growth direction. These authors have also performed a detailed analysis considering the effects of the spin-dependent boundary conditions (along the growth axis of the well) on the SO energy splittings. They found that the inclusion of the spin-dependent boundary conditions gives rise to small corrections to the calculated SO energy splittings, with more sizable corrections for heavily doped ($>10^{12}$ cm^{-2}) narrower band-gap heterostructures (e.g. $InAs/In_{0.8}Al_{0.2}As$). However, the influence of the spin-dependent boundary conditions on the Rashba couplings (α) is not mentioned in their study. We believe that the inclusion of the spin-dependent boundary conditions (along the growth) in our problem will not alter the results in any essential way (certainly not qualitatively); For an alternate description of the Rashba effect using a multiband approach see U. Ekenberg and D. M. Gvozdic, arXiv:0801.0089 (unpublished). As these authors emphasize, the contrasts between these two descriptions deserve further study.

[29] For a 14×14 $\mathbf{k}\cdot\mathbf{p}$ model which accounts for the Rashba and Dresselhaus terms on the same footing, see, e.g. F. V. Kyrychenko, C. A. Ullrich, and I. D'Amico, J. Magn. Magn. Mater. (to be published); arXiv:0710.2866 (unpublished). These authors investigate whether the intersubband SO coupling discussed here should be accounted for when extracting the spin Coulomb drag from intersubband spin plasmon linewidths; they conclude it has a negligible effect on that property.

[30] R. J. Warburton, C. Gauer, A. Wixforth, J. P. Kotthaus, B. Brar, and H. Kroemer, Phys. Rev. B **53**, 7903 (1996); E. L. Ivchenko and S. A. Tarasenko, JETP **99**, 379 (2004); J. B. Khurgin, Appl. Phys. Lett. **88**, 123511 (2006), have investigated optical intersubband couplings (dipolar approximation) in quantum wells. Even though these authors have taken into account the spin-orbit interaction (via the $\mathbf{k}\cdot\mathbf{p}$ approximation) when calculating these light-induced transitions, we emphasize that the intersubband coupling we consider in our work [Eqs. (34)–(37) or Eqs. (40)–(43)] is of a different nature. By looking at, e.g., the intersubband matrix element in Eqs. (15)–(17) in the work of Ivchenko and Tarasenko, we can see that their matrix element (i) is proportional to the amplitude of the electromagnetic vector potential A and, more importantly, that (ii) it is independent of the Kane matrix element P. Our intersubband coupling, on the other hand, is directly proportional to the Kane matrix element P [defined in our Eq. (10)] and does not depend on a vector potential A (we do not treat optical absorption, i.e., $A=0$ in our work). We believe, however, that intersubband light absorption may provide an interesting means to experimentally probe and contrast the spin-orbit interactions (in the single and double wells) investigated here. This issue will be addressed in a future work.

[31] R. Enderlein and N. J. Horing, *Fundamentals of Semiconductor Physics and Devices* (World Scientific, Singapore, 1999).

[32] T. Koga, J. Nitta, T. Akazaki, and H. Takayanagi, Phys. Rev. Lett. **89**, 046801 (2002).

[33] T. Koga, Y. Sekine, and J. Nitta, Phys. Rev. B **74**, 041302(R) (2006).

[34] R. Fletcher, M. Tsaousidou, T. Smith, P. T. Coleridge, Z. R. Wasilewski, and Y. Feng, Phys. Rev. B **71**, 155310 (2005).

[35] For a detailed calculation of the Rashba SO-induced changes of the quasiparticle effective mass in a two-dimensional Fermi liquid, see D. S. Saraga and D. Loss, Phys. Rev. B **72**, 195319 (2005).

[36] B. V. Numerov, Mon. Not. R. Astron. Soc. **84**, 592 (1924).

[37] J. M. Blatt, J. Comput. Phys. **1**, 382 (1967).

[38] P. C. Chow, Am. J. Phys. **40**, 730 (1972).

[39] R. P. Agarwal and Y. M. Wang, Comput. Math. Appl. **42**, 561 (2001).

[40] E. Bernardes, arXiv:0712.1706 (unpublished).

[41] L. J. Slater, in *Handbook of Mathematical Functions*, edited by M. Abramowitz and I. A. Stegun (Dover, New York, 1964), p. 503.

[42] G. A. Samara, Phys. Rev. B **27**, 3494 (1983).

[43] *Handbook of Chemistry and Physics*, edited by D. R. Lide (CRC, Boca Raton, 2004).